https://doi.org/10.5194/essd-2025-738
Preprint. Discussion started: 23 December 2025

Open Access Earth System Science Data Discussions

Global Gridded Air-sea Oxygen Flux Inferred from a Machine Learning-based Dissolved Oxygen Product

Yuming Jin[1,2], Britton B. Stephens[1], Eric J. Morgan[3], Manfredi Manizza[3,a], Jonathan Sharp[4,5]

[1]Earth Observing Laboratory, NSF National Center for Atmospheric Research, Boulder, CO, USA

[2]Advanced Study Program, NSF National Center for Atmospheric Research, Boulder, CO, USA

[3]Geosciences Research Division, Scripps Institution of Oceanography, University of California, San Diego, La Jolla, CA, USA

[4]Cooperative Institute for Climate, Ocean, and Ecosystem Studies, University of Washington, Seattle, WA 98105, USA

[5]Pacific Marine Environmental Laboratory, National Oceanic and Atmospheric Administration, Seattle, WA 98115, USA

[a]Now at: National Institute of Oceanography and Applied Geophysics - OGS, Trieste, Italy

Correspondence: Yuming Jin (yumingjin@ucar.edu)

https://doi.org/10.5194/essd-2025-738
Preprint. Discussion started: 23 December 2025

Open Access Earth System Science Data Discussions

Abstract

We present estimates of the monthly open ocean air-sea O_2 flux from 2004 to 2024 on a 1°×1° grid spanning 64.5°S to 79.5°N. The flux is computed using 4-dimensional ocean dissolved oxygen (DO) fields derived from Argo float and shipboard observations via machine learning algorithms (GOBAI-O_2, Sharp et al., 2023). Flux uncertainties are quantified by generating a large ensemble of flux estimates, first propagating errors from the dissolved oxygen product, then computing fluxes across all combinations of three gas exchange parameterizations that account for bubble-mediated flux and three wind products. We apply DO adjustments to align our resolved global annual mean fluxes with those derived from scaling global ocean heat uptake and regional annual mean fluxes with those derived from ocean inversions. Our results show larger seasonal flux variations at high latitudes than at low latitudes, with clear differences between major ocean basins. Both adjusted and unadjusted annual mean flux estimates exhibit strong ocean O_2 sinks at high latitudes, weak sources in the low-to-mid latitude subtropics, and weak sinks near the Equator. The annual mean adjustment significantly enhances ocean O_2 uptake in the northern high latitudes and tropical regions while reducing outgassing in the northern subtropics. We evaluate our flux seasonal cycles and annual mean values by comparing forward transport simulations with atmospheric O_2 observations from global airborne surveys and surface sampling stations. The simulations reproduce the observed mean seasonal cycles well, but some differences remain in the annual mean latitudinal gradients. We analyze fractional variance contributions from DO, wind, and gas exchange scheme uncertainties and their interactions at regional and hemispheric scales for both climatological monthly and annual mean fluxes. This dataset marks a major improvement over existing air-sea O_2 flux products, as it includes the resolution of interannual variability in the flux seasonal cycle, the use of advanced machine learning-based DO fields that better represent complex spatial and temporal patterns, and robust uncertainty quantification across various scales.

Short Summary

We produce monthly air-sea O_2 flux estimates (2004-2024) on a 1°×1° grid using machine learning-based dissolved oxygen fields (GOBAI-O_2, Sharp et al., 2023). Fluxes are calculated with multiple gas exchange schemes and wind products, then constrained to match independent

https://doi.org/10.5194/essd-2025-738
Preprint. Discussion started: 23 December 2025

regional to global annual mean fluxes estimates. We evaluate flux seasonal cycles and annual patterns against atmospheric O_2 observations and quantify flux uncertainties from multiple sources.

1 Introduction

Accurate estimates of air-sea O_2 fluxes have the potential to place critical constraints on ocean productivity, CO_2 uptake, and heat flux (e.g., Keeling et al., 1993, 2010; Keeling and Manning, 2014), but large biases and uncertainties exist in current estimates (Jin et al., 2023). Air-sea O_2 fluxes are driven by surface ocean DO concentration changes resulting from physical and biogeochemical processes. Because oxygen has low solubility in seawater, changes in surface ocean DO create large disequilibria with the atmosphere, producing strong gas exchange as the ocean-atmosphere system seeks equilibrium (Garcia and Gordon, 1992).

The air-sea flux of O_2 exhibits pronounced seasonal variability driven by seasonal changes in solubility, biological activity, and ocean mixing (Redfield, 1948). Extratropical oceans outgas O_2 from spring to summer, and takes up O_2 from fall to winter (Garcia and Keeling, 2001; Najjar and Keeling, 2000). During the growing season, enhanced photosynthesis increases oxygen production in surface waters, while summer thermal stratification limits vertical mixing, often creating oxygen supersaturation that drives outgassing to the atmosphere (Emerson, 1987; Najjar and Keeling, 1997). In the winter, diminished biological production and ventilation of oxygen-depleted deep waters lead to oxygen uptake from the atmosphere (Bushinsky and Emerson, 2018; Redfield, 1948). Thermal forcing reinforces these drivers, as seasonal air-sea heat fluxes directly affect O_2 solubility (Weiss, 1970). Summer warming reduces solubility and reinforces O_2 outgassing, while winter cooling enhances oceanic O_2 uptake (Keeling and Shertz, 1992).

Although seasonal fluxes largely compensate on annual time scales, the global ocean is a weak source of O_2 to the atmosphere due to ocean heat uptake, which reduces oxygen solubility, and warming-induced stratification, which reduces both the upwelling of nutrients from the deep ocean and the downward transport of oxygen-rich surface waters to depth (Breitburg et al., 2018; Keeling et al., 2010; Keeling and Garcia, 2002; Schmidtko et al., 2017). Accurately quantifying

https://doi.org/10.5194/essd-2025-738
Preprint. Discussion started: 23 December 2025

this annual flux remains challenging because its magnitude is small compared to both the seasonal cycle and interannual variations.

Several attempts have been made to produce global-scale gridded seasonal air-sea O_2 fluxes from hydrographic data, though these efforts have only succeeded in resolving climatological seasonal fluxes and without including the global annual mean flux. Najjar and Keeling (1997) created a monthly climatology of surface ocean DO anomalies using spatial and temporal interpolation of historical DO data collected between 1900-1994, further scaled by maps of sea surface temperature (SST). Keeling et al. (1998b) then computed air-sea fluxes using these DO anomalies along with wind speed data and gas exchange velocity formulations, applying corrections to DO anomalies for sea level atmospheric pressure and sea surface skin temperature effects and rescaling DO anomalies by SST. Najjar and Keeling (2000) later improved this approach by adding corrections for DO anomalies caused by air bubble injection and by using different skin temperature corrections. These methods captured the hemispheric-scale air-sea O_2 flux seasonal cycle, but significantly underestimated the amplitude of high-latitude flux, when compared to values inferred from baseline surface station observations (Najjar and Keeling, 2000).

Garcia and Keeling (2001, referred to as GK01) presented an important advancement by developing a new methodology that binned DO data by increments in seasonal air-sea heat flux anomalies. This method takes advantage of a tight relationship between O_2 flux and heat flux, regardless of whether the O_2 flux is driven by thermal or biological processes (Garcia and Keeling, 2001; Keeling et al., 1993). However, when compared to hemispheric fluxes derived from airborne atmospheric O_2 measurements, this product still shows clear biases that indicate limitations in sampling coverage and O_2 flux to heat flux assumptions (Bent, 2014; Jin et al., 2023, 2025). These biases include underestimated seasonal flux amplitude in both hemispheres, underestimated northern wintertime O_2 uptake, a missing late-summer O_2 outgassing period in the Northern Hemisphere, an unresolved seasonal flux asymmetry between hemispheres, and flux phase timing approximately 2 weeks too early in the Southern Hemisphere.

Recently, advances in machine learning (ML) techniques have revolutionized the ability to interpolate sparse ocean measurements into comprehensive gridded products, thus enabling improved calculations of regional and global dissolved O_2 across seasonal to interannual

https://doi.org/10.5194/essd-2025-738
Preprint. Discussion started: 23 December 2025

timescales. GOBAI-O_2 (Sharp et al., 2023), a recent ML-based product, establishes relationships between DO collected from Argo floats and ships and physical variables including temperature, salinity, location, and time. This product successfully generates monthly 3D maps of DO to 2000 meters depth from 2004 onwards with high accuracy. This product offers the opportunity to place new constraints on air-sea O_2 fluxes. It is important to note that there are other gridded DO products based on either ML methods (Huang et al., 2023; Ito et al., 2024) or other statistical methods (Garcia et al., 2024; Gouretski et al., 2024; Roach and Bindoff, 2023; Zhou et al., 2022), but here we choose to focus only on GOBAI-O_2, because it provides detailed component-level DO uncertainty estimates, which are essential for robust uncertainty propagation in our flux calculations.

Here we utilize the latest GOBAI-O_2 version 2.3 (v2.3) to produce the first multi-decadal, seasonally resolved and interannually varying monthly gridded air-sea O_2 flux product. We generate a large ensemble of DO estimates by accounting for measurement and method uncertainties from the GOBAI-O_2 product. We then calculate fluxes using three gas-exchange schemes that consider both diffusive and bubble-mediated gas exchange, combined with three wind products. This approach yields a large ensemble of 9000 flux estimates that captures uncertainties from DO fields, gas exchange parameterizations, and wind speeds. We calculate annual mean DO concentration adjustments to match annual mean fluxes with global annual fluxes derived from scaling ocean heat uptake (Keeling and Manning, 2014), and regional annual fluxes derived from five ocean inversions (Resplandy et al., 2016). These adjustments are then applied to the DO fields, and the fluxes are recalculated. We provide a detailed analysis to identify the main sources of flux uncertainty for each ocean basin across different time scales. To evaluate our flux product, we transport the resolved fluxes in an atmospheric transport model and compare them with observations from global airborne surveys and surface stations. Our flux product performs well against these independent observation metrics. The flux product has broad potential applications in studies of marine biogeochemistry and the global carbon cycle.

https://doi.org/10.5194/essd-2025-738
Preprint. Discussion started: 23 December 2025

2 Methods

2.1 Machine-learning-based dissolved oxygen product

We calculate monthly air-sea O_2 flux using mixed-layer ocean DO data from the GOBAI-O_2 dataset (Sharp et al., 2023). The dataset covers about 86% of the global ocean (by surface area) from -179.5° to 179.5° longitude and -64.5° to 79.5° latitude on a 1°×1° grid, extending from the surface to 2000-m depth. GOBAI-O_2 is an observation-based product of 3D gridded DO fields, constructed by training feed-forward neural networks (FFNNs) to relate sparse DO observations from BGC Argo float-mounted sensors (Bittig et al., 2022) and discrete measurements from ship-based surveys (GLODAPv2.2022, Olsen et al., 2016) with input variables including temperature, salinity, and spatiotemporal information (latitude, longitude, year, and day of year). The trained FFNNs are applied to Argo-based monthly gridded values (Roemmich and Gilson, 2009) of temperature, salinity, and potential density anomaly, along with pressure, bottom depth, and spatiotemporal information.

We use GOBAI-O_2 v2.3 (Sharp et al., 2025), which extends from 2004 through 2024 at monthly resolution, and employs an updated methodology compared to the earlier version (v2.1) described in Sharp et al. (2023). The v2.3 methodology uses a Gaussian mixture model, a statistical clustering algorithm that identifies regions with similar oceanographic characteristics, to partition the global ocean into distinct clusters based on sparse observations from BGC Argo floats and ship-based measurements. Within each cluster, an ensemble of three FFNNs is trained to capture region-specific dependencies of DO on other input variables and quantify algorithm uncertainty. This clustering approach allows each FFNN ensemble to be trained on data with reduced variability, improving prediction accuracy compared to a single global model.

The v2.3 update also includes improved bias adjustment procedures for float and ship measurements to enhance agreement between the two data types and reduce systematic offsets. Unlike previous versions, v2.3 does not use random forest regressions (RFRs). Model simulation tests indicated that although RFRs were effective at estimating DO for withheld data similar to the training data, they exhibited high errors when encountering data significantly outside the spatiotemporal bounds of the training data.

https://doi.org/10.5194/essd-2025-738
Preprint. Discussion started: 23 December 2025

The earlier GOBAI-O_2 v2.1 product was evaluated by comparing output from validation versions of its algorithms to withheld observational data (Sharp et al., 2023). The evaluation showed no systematic biases, with a minimal global mean offset of -0.2 µmol kg^{-1}, and global mean root-mean-square differences (RMSD) of 8.8 µmol kg^{-1}. New evaluation statistics for GOBAI-O_2 v2.3 with an even more comprehensive *k*-fold cross-validation approach that tests every observational data point show a global mean offset of 0.0 µmol kg^{-1}, and global mean RMSD of 8.3 µmol kg^{-1}. Errors can be larger (or smaller) when analyzed for individual regions, and a comprehensive uncertainty estimate for GOBAI-O_2 is available and incorporated into our analysis (see Section 2.2).

2.2 Mixed-layer DO large ensemble

We calculate mixed-layer averages of DO, temperature, and salinity to obtain representative surface properties for O_2 flux calculations. mixed-layer depth (MLD) is defined as the depth at which potential density exceeds the potential density at 10 m depth by 0.03 kg m^{-3} (De Boyer Montégut et al., 2004). Potential density is calculated following the Thermodynamic Equation Of Seawater - 2010 (TEOS-10) standard, using depth, and temperature and salinity from EN4, which are also used as the input variable in GOBAI-O_2.

We generate a large ensemble (1000 members) of 2D (longitude × latitude) gridded monthly mixed-layer-averaged DO fields, based on the reported GOBAI-O_2 uncertainties. The total uncertainty consists of three components reported individually for each monthly 3D grid (longitude × latitude × depth), which are measurement uncertainty, representation/gridding uncertainty, and algorithm uncertainty. We combine representation/gridding uncertainty with algorithm uncertainty into a single method uncertainty term using a root sum of squares.

For each monthly 2D grid cell, which combines estimates averaged from multiple depths, measurement and method uncertainty are calculated as a scaled sum of uncertainties across vertical grid cells within the MLD, following

$$\mathrm{unc}^{\mathrm{s}}(\mathrm{i},\mathrm{t}) = \sqrt{\frac{\sum \sigma_{\mathrm{j}}^2(\mathrm{i},\mathrm{t}) \cdot (1 + (\mathrm{n}-1)\rho)}{\mathrm{n}^2}}, \quad (1)$$

https://doi.org/10.5194/essd-2025-738
Preprint. Discussion started: 23 December 2025

where s denotes the source of uncertainty, i denotes each 2D location, t denotes each month, j denotes the vertical grid level, ρ denotes correlation, and n denotes the total number of vertical grid levels for each 2D location (i) and time (t) within the MLD. We assume that method uncertainty has a vertical correlation of 0.8, while measurement uncertainty is vertically uncorrelated. We then calculate separate monthly climatological averages of measurement and method uncertainty for each 2D grid cell.

For each ensemble member, we add perturbations to the mean mixed-layer-averaged DO field, where the perturbations consist of systematic method uncertainty that is assumed to be correlated spatially with a 500 km exponential decay scale and temporally with a 3-month exponential decay scale. It also includes random climatological measurement uncertainty applied independently to each 2D grid point and each time step without spatial and temporal correlation.

2.3 Air-sea O_2 flux calculation

We calculate "raw" air-sea O_2 fluxes using three gas exchange parameterization schemes (Appendix A) that consider bubble-mediated fluxes, which are from Woolf (1997, referred to as W97), Liang et al. (2013, referred to as L13), and Stanley et al. (2009, referred to as S09). We use three 2-m wind products from CCMP (Mears et al., 2022), ERA-5 (Hersbach et al., 2020), and JRA-3Q (Kosaka et al., 2024). The combination of three parameterization schemes and three wind products generates nine flux models. Each flux model is applied to the DO ensemble (Section 2.2) from GOBAI-O_2, resulting in 9000 flux estimates.

The net air-sea O_2 flux (F_T) calculation consists of O_2 diffusive flux (F_s) and flux due to bubbles (F_b), following

$$F_T = (F_s + F_b) \cdot (1 - c_{ice}), \quad (2)$$

where c_{ice} is the monthly sea-ice fraction from HadISST (Rayner et al., 2003). In the L13 and S09 schemes, F_b is further decomposed into flux due to large bubbles that do not collapse (F_p) and flux due to small bubbles that collapse (F_c), following

$$F_b = F_p + F_c. \quad (3)$$

https://doi.org/10.5194/essd-2025-738
Preprint. Discussion started: 23 December 2025


Open Access Earth System Science Data Discussions

F_s is calculated as the product of O_2 anomaly ($\Delta[O_2]$) and gas exchange velocity (k_s), which is different in each scheme. The anomaly is calculated as the deviation of DO from GOBAI ($[O_2]_{adj}$) plus an annual mean adjustment term (δ) against O_2 saturation ($[O_2^{sat}]$), following

$$\Delta[O_2] = [O_2] + \delta - [O_2^{sat}]. \quad (4)$$

This adjustment term constrains the regional and global annual mean O_2 fluxes based on independent observation-based estimates as described in the following Section 2.4.

F_p in Eq. 3 is calculated as the product of the gas exchange coefficient across the large bubble interface and $\Delta[O_2]$. F_c is calculated as the product of a mass transfer coefficient (k_c) and a constant O_2 atmospheric mole fraction (X^{O_2} = 0.2094).

Full descriptions of the three gas exchange schemes are presented in Appendix A, following Emerson and Bushinsky (2016).

2.4 Annual mean DO adjustments

Calculating the annual mean O_2 flux from surface ocean measurements is challenging because it requires detecting a small net signal against much larger seasonal variations that typically cancel out over the seasonal cycle. The annual mean flux is therefore particularly sensitive to methodological choices (e.g., gas exchange scheme) and to corrections for DO anomalies from sea level pressure variations and skin temperature effects (Najjar and Keeling, 2000).

Here we apply independent constraints to force the global annual mean flux to equal smoothed annually-varying values derived from scaling ocean heat content changes, which average to 61 Tmol $year^{-1}$ over 2004-2024. The O_2 flux to heat flux relationship is primarily valid on the decadal timescale and at global scales (Keeling and Garcia, 2002). Details are presented in Appendix B.

We also force regional annual mean fluxes (six ocean regions, Fig. B1) to match those from a randomly selected one of the five ocean inversions (Table B2) reported in Resplandy et al. (2016). We optimize the constant adjustments (δ), and add them to each DO ensemble member (Eq. 4). This constant DO adjustment term varies for each of the six ocean regions, each year, and each flux ensemble member. This adjustment method is adapted from an early study of

https://doi.org/10.5194/essd-2025-738
Preprint. Discussion started: 23 December 2025

Najjar and Keeling (2000), who applied a globally uniform adjustment of 0.7 μmol kg^{-1} to their gridded DO datasets to force zero global annual mean flux. These annual adjustments effectively remove interannual variability (IAV) in the ensemble mean annual mean fluxes in our product, while the smoothed global mean flux trend and IAV in seasonal cycles are preserved. A previous study suggests that the IAV of global annual mean O_2 flux is driven primarily by ocean ventilation rather than ocean heat flux on this timescale (Hamme and Keeling, 2008). We present further details on the adjustments and their uncertainty in Appendix B.

2.5 Flux uncertainty

We estimate gridded monthly flux uncertainty using a large flux ensemble (9000 members) that incorporates DO uncertainty, including additional uncertainty from annual mean DO adjustments, gas exchange uncertainty, and wind uncertainty. In our air-sea O_2 flux product, we report the 1-σ uncertainty for each grid cell as the standard deviation across all ensemble members. We report regional average fluxes and their uncertainties for 18 RECCAP2 ocean regions and both hemispheres at monthly climatological and annual timescales. Regional uncertainty is calculated as the standard deviation of area-weighted average fluxes across all ensemble members for each region.

We quantify the fractional variance contribution of each uncertainty source to total flux uncertainty using a three-way factorial mixed-effects analysis of variance (ANOVA). The model is implemented with restricted maximum likelihood estimation (REML) in R (Bates et al., 2015). The model treats the use of three different wind products and three gas exchange parameterization schemes as fixed effects, while DO fields (1000 members) are included as a random effect. The model also includes interaction terms that capture methodological interactions between wind and gas exchange parameterization, as well as DO-dependent interactions that represent how methodological uncertainties vary across different DO conditions. Variance components from the fitted model determine the percentage contribution of each source to total uncertainty. This analysis is conducted for 18 RECCAP2 ocean regions and both hemispheres at monthly climatological and annual timescales.

https://doi.org/10.5194/essd-2025-738
Preprint. Discussion started: 23 December 2025

2.6 Flux evaluation

We evaluate our flux products by transporting the gridded ensemble mean air-sea O_2 flux in the TM3 atmospheric transport model (Heimann and Körner, 2003). For ocean grid cells not covered by the GOBAI-O_2 product, we set the flux to zero. TM3 is an offline tracer transport model driven by NCEP reanalysis (Kalnay et al., 1996), run on a spatial resolution of 5° longitude, 3.8° latitude and 19 vertical levels. The TM3 forward transport produces station and airborne co-samples at measurement locations and times for direct comparison with observations. We focus specifically on evaluating the seasonal cycle and adjusted annual mean flux.

We compare TM3 simulations with measurements of atmospheric potential oxygen (APO, Stephens et al., 1998) that are further corrected to represent changes due to air-sea O_2 flux alone (Appendix C). We refer to this corrected atmospheric tracer as O_2^{ocn} and its atmospheric abundance as ΔO_2^{ocn}. APO is defined following

$$\mathrm{APO} = \delta(\mathrm{O_2/N_2}) + \frac{1.1}{\mathrm{X_{O_2}}}(\mathrm{CO_2} - 350), \tag{5}$$

where $\delta(O_2/N_2)$ is measured as deviations in the O_2 to N_2 ratio relative to an arbitrary reference multiplied by 10^6 and expressed in units of per meg, CO_2 is the measured atmospheric concentration of CO_2 in ppm units, X_{O_2} is the mole fraction of O_2 in the atmosphere (0.2094), and the constant 1.1 is an approximation of the exchange ratio of O_2 production/consumption to CO_2 consumption/production from the terrestrial biosphere (Severinghaus, 1995). The ppm unit for CO_2 is converted to equivalent per meg units by dividing by X_{O_2} (Keeling et al., 1998a).

2.7 Atmospheric measurements

We use airborne APO data, calculated from O_2 and CO_2 measurements made by the NCAR Atmospheric Oxygen instrument (AO2) and NCAR / Scripps Medusa Flask Sampler (Stephens et al., 2021g), from three global to regional aircraft surveys (Stephens et al., 2018; Thompson et al., 2022; Wofsy, 2011) to evaluate flux seasonal cycles and annual mean latitudinal gradients. These airborne data are available in separate months spanning 2009 to 2018, with sufficient temporal coverage to resolve a climatological seasonal cycle and provide nearly pole-to-pole coverage (Fig. S1) from the boundary layer to above the tropopause (Jin et al., 2023). We group

https://doi.org/10.5194/essd-2025-738
Preprint. Discussion started: 23 December 2025

289 10-second airborne data into eight latitude bands from 80°S to 80°N at 20° intervals and average
290 over the 1000- to 400-mbar range to produce tropospheric-average estimates. Prior to grouping,
291 all stratospheric data are excluded, with stratospheric air defined by observed water vapor less
292 than 50 ppm and either O_3 greater than 150 ppb or N_2O (detrended to the reference year 2009)
293 less than 319 ppb (Jin et al., 2021). Water vapor and O_3 were measured by the NOAA UCATS
294 instrument (Hintsa et al., 2021) and were interpolated to a 10-second resolution. N_2O was
295 measured by the Harvard QCLS instrument (Santoni et al., 2014). We also exclude data within
296 the boundary layer and during missed approach (Jin et al., 2021).

297 We also use APO measurements made on flasks collected at 10 sampling sites within the Scripps
298 O_2 Program surface flask network (Keeling, 2019) to evaluate global annual mean fluxes. These
299 stations extend from the South Pole to 82.3°N, primarily along the Pacific, with data available as
300 early as 1991 at roughly bi-monthly resolution for each station (Fig. S1).

301 For each measurement, we correct APO observations for non-oceanic O_2 flux components to
302 derive ΔO_2^{ocn}. These corrections include air-sea N_2 and CO_2 fluxes, fossil fuel CO_2 emissions
303 and O_2 uptake (full derivation in Appendix C). We use two air-sea N_2 flux estimates, two air-sea
304 CO_2 flux estimates, and two fossil fuel O_2 and CO_2 flux estimates, all transported by four
305 different transport models, yielding 32 unique correction combinations. These flux transport
306 outputs are available from a previous APO model intercomparison project (Jin et al., 2025) that
307 provides direct co-sampling at observation locations and times. These 32 corrections are applied
308 to a large ensemble (1000 members) of observations, yielding 32,000 members to quantify
309 correction uncertainty. It is important to note that these corrections have only minimal impact on
310 the ΔO_2^{ocn} seasonal cycle (Fig. C1), but are important for determining the trend in annual mean
311 ΔO_2^{ocn} (Section 3.2.2).

312 **3 Results and Discussion**

313 **3.1 Air-sea O_2 flux**

314 We present gridded seasonal flux climatology maps and uncertainty in Fig. 1, as well as monthly
315 zonal-average fluxes (2004-2024 average) and uncertainties in Fig. S1. Our analysis focuses on
316 examining seasonal flux patterns (Section 3.1.1) and annual means (Section 3.1.2). Fig. 2

https://doi.org/10.5194/essd-2025-738
Preprint. Discussion started: 23 December 2025

317 presents monthly flux climatologies for 18 RECCAP2 regions plus Northern and Southern
318 Hemisphere averages. Fig. 3 shows flux seasonal cycle amplitude (SCA) and annual mean
319 values, presented as both gridded fields and zonal averages with associated uncertainties. Fig. 4
320 compares annual mean fluxes between regions, showing results both with and without annual
321 adjustments. Fig. 5 analyzes fractional contributions of each uncertainty source to total flux
322 uncertainty for climatological seasonal cycles and annual means across all 20 regions.

323 **3.1.1 Flux seasonal variation**

324 Our air-sea O_2 flux exhibits clear seasonal patterns. In each hemisphere (Figs. 1 and 2S-T), there
325 is net outgassing during summer and net uptake during winter, with rapid transitions between
326 seasons. This pattern is consistent with the combined influence of thermal and biological forcing
327 that enhances the seasonal flux cycle. However, the two hemispheres show clear asymmetry in
328 seasonal flux phases (Figs. 2S-T). The Northern Hemisphere exhibits prolonged summer
329 outgassing from April to November (7 months) with two distinct peaks in June and September.
330 In contrast, the Southern Hemisphere shows only a slightly longer outgassing period than its
331 uptake period, without a clear double-peak structure. Despite this temporal asymmetry, the two
332 hemispheres exhibit nearly identical per-area flux SCAs, with 17.7±1.48 mol m^{-2} yr^{-1} in the north
333 and 17.9±1.48 mol m^{-2} yr^{-1} in the south (Table 1). When accounting for the larger ocean area in
334 the Southern Hemisphere, however, the total SCA in the south (3385±280.2 Tmol yr^{-1}) is
335 significantly larger than that in the north (2257±187.2 Tmol yr^{-1}).

336 Within each hemisphere, flux SCA is larger at mid-to-high latitudes (Figs. 2A-C) due to stronger
337 seasonal variations in SST, heat flux, and biological production that drives larger seasonal
338 changes in surface ocean DO. In the Northern Hemisphere, flux SCA peaks at 58.5°N
339 (88.3±10.16 mol m^{-2} yr^{-1}, Fig. 3C), driven by significant seasonal flux variations over the western
340 North Pacific and western North Atlantic (Figs. 2A and G, 3A). SCA is larger over the subpolar
341 North Atlantic (70.0±7.44 mol m^{-2} yr^{-1}, Fig. 2G) than the subpolar North Pacific (56.2±5.35 mol
342 m^{-2} yr^{-1}, Fig. 2A) due to stronger wintertime O_2 uptake, likely a thermal signal associated with
343 North Atlantic deep-water formation. North of 58.5°N, SCA averages 57.9 mol m^{-2} yr^{-1} between
344 60°N and 79.5°N. We note that the O_2 flux over the Arctic Ocean and Bering Strait is unavailable
345 in our product due to the lack of GOBAI-O_2 data.

https://doi.org/10.5194/essd-2025-738
Preprint. Discussion started: 23 December 2025

Moving southward in the North Pacific and North Atlantic, SCA values decrease from subpolar regions to subtropical regions (Figs. 2B, C, H, I, and Table 1). The onset of net O_2 outgassing and the peak timing both shift earlier from high to low latitudes, likely due to earlier bloom onset and thermal changes at lower latitudes. Broad summer outgassing plateaus are evident over both the North Pacific and Atlantic (Figs. 2A, B, H), particularly prominent in Pacific subpolar and subtropical-seasonally-stratified regions (Fig. 2A-B) and the North Atlantic subtropical-permanently-stratified region (Fig. 2H). These "plateaus" and secondary outgassing peaks result from the formation of a shallow oxygen maximum zone (SOM), which has been observed over the North Pacific (Hayward, 1994; Ishidoya et al., 2016). The SOM forms when strong summer stratification traps photosynthetically produced O_2 below the mixed-layer, delaying outgassing until fall when the mixed-layer deepens.

In the Southern Hemisphere, flux SCA shows double peaks of 39.0±4.71 mol m^{-2} yr^{-1} at 54.5°S and 39.6±3.67 mol m^{-2} yr^{-1} at 44.5°S (Fig. 3C). Note that flux data south of 64.5°S are unavailable. SCA remains comparably large over the Southern Ocean subpolar region (SO-SPSS, 38.2±4.56 mol m^{-2} yr^{-1}, Fig. 2Q) and subtropics (35.2±3.00 mol m^{-2} yr^{-1}, Fig. 2P), although both values are significantly smaller than those in the subpolar North Pacific and North Atlantic. South of this subpolar region, the Southern Ocean seasonally ice-covered zone north of 64.5°S shows reduced SCA (26.6±3.44 mol m^{-2} yr^{-1}, Fig. 2R) due to winter ice coverage that reduces the net O_2 sink. Equatorward, SCA is considerably smaller over permanently-stratified regions, with values of 9.1±0.70 mol m^{-2} yr^{-1} in the Pacific (Fig. 2F), 12.8±0.92 mol m^{-2} yr^{-1} in the Atlantic (Fig. 2K), and 6.0±0.67 mol m^{-2} yr^{-1} in the Southern Indian Ocean (Fig. 2O). As in the Northern Hemisphere, the Southern Hemisphere exhibits earlier phase shifts in outgassing onset and peak timing from high to low latitudes. However, unlike the Northern Hemisphere, the Southern Hemisphere does not exhibit pronounced "summer plateaus", likely because deeper mixed-layers prevent formation of the SOM (Jin et al., 2023).

Over the equatorial region, the Eastern Equatorial Pacific (Fig. 2E), Equatorial Atlantic (Fig. 2J), and Equatorial Indian Ocean (Fig. 2L) exhibit seasonal flux patterns that generally follow the Southern Hemisphere cycle. However, maximum outgassing occurs approximately three months later in the Equatorial Atlantic (Fig. 2J) and Eastern Equatorial Pacific (Fig. 2E) compared to the Southern Hemisphere pattern. In the Arabian Sea (Fig. 2L) and Bay of Bengal (Fig. 2M),

https://doi.org/10.5194/essd-2025-738
Preprint. Discussion started: 23 December 2025

seasonal flux patterns exhibit double peaks in May and November, with the timing of maximum uptake remaining generally consistent with the Southern Hemisphere flux cycle. In contrast, the Western Equatorial Pacific (Fig. 2D) shows minimal seasonal flux variation, with persistent O_2 outgassing throughout the year. The seasonal cycle over the Eastern Equatorial Pacific is primarily driven by upwelling of cold deep water. A similar upwelling mechanism operates over the Eastern Equatorial Atlantic but with smaller magnitude. In the Arabian Sea and Bay of Bengal, upwelling during the summer monsoon brings cold water to the surface through Ekman-driven vertical transport (Schott and McCreary, 2001).

Our flux estimates show no significant ($p < 0.05$) SCA trends over most RECCAP2 regions (Fig. S3), except in the Southern Ocean subtropical seasonally-stratified zone (Fig. S3P), which exhibits a trend of 2.2 mol m^{-2} yr^{-1} $decade^{-1}$.

Air-sea O_2 flux calculations are sensitive to the choice of gas exchange parameterization scheme. Figure A1 shows that flux estimates vary considerably among different schemes, particularly at the high latitudes and during winter when strong winds amplify gas exchange rates. Generally, the L13 scheme produces the smallest SCA due to its calculation of weaker wintertime O_2 uptake, while the W97 scheme yields the largest SCA. Over the Southern Ocean subpolar region (Fig. A1Q), the wintertime peak O_2 uptake in August varies by approximately 9 mol m^{-1} yr^{-1} around an ensemble mean of ~34 mol m^{-2} yr^{-1}. The impact of parameterization choice is much smaller over low-latitude regions where wind speeds are generally lower.

Flux calculations are less sensitive to the choice of wind product. Figure A2 shows that the hemispheric-scale O_2 monthly flux climatologies are highly consistent across the three wind products used. However, larger deviations occur for individual regions. Over the Southern Ocean ice-covered zone (Fig. A2R), JRA-3Q produces the largest wintertime O_2 uptake. In other high-latitude regions of both hemispheres, wintertime uptake is larger when using the CCMP wind product, but remains close to the JRA-3Q-based estimate. Over the Bay of Bengal (Fig. A2M), JRA-3Q produces much smaller JJA outgassing compared to the other wind products. These wind products show considerable variation in this region, likely reflecting large uncertainty in surface winds during the monsoon season. Gas exchange uncertainty and wind uncertainty interact nonlinearly, amplifying the total uncertainty. This interaction is particularly

https://doi.org/10.5194/essd-2025-738
Preprint. Discussion started: 23 December 2025

pronounced when testing gas exchange schemes with wind products that have faster wind speeds, as gas transfer velocity scales nonlinearly with wind speed.

The annual mean DO adjustment alters the seasonal flux cycle through the interaction between the temporally constant DO adjustments and seasonally varying wind speeds in the gas exchange parameterization (Fig. B3). In the northern high-latitude oceans, where the DO reductions from the adjustment are largest and winter wind speeds are much stronger than in summer, the adjustment significantly increases the seasonal cycle amplitude (SCA) by up to 10%. This increase results from enhanced wintertime O_2 uptake that exceeds the reduction in summertime outgassing following the adjustment. The North Atlantic subpolar region experiences the largest SCA change, with an increase of 5.7 mol m^{-2} yr^{-1}. In contrast, SCA remains largely unchanged in the southern high latitudes due to the smaller DO adjustments in these regions. Across most regions, the annual mean DO adjustment also reduces the ensemble standard deviation (1-σ) of SCA.

We show that the total uncertainty in climatological monthly flux is dominated by either DO uncertainty or gas exchange uncertainty in most regions and months (Fig. 5). In the high-latitude regions of both hemispheres (Fig. 5A, B, G, H, P, Q, R), total uncertainty is dominated by gas exchange uncertainty throughout most of the year, except when net fluxes approach zero, during which DO uncertainty dominates. In mid-latitude subtropical regions of both hemispheres (Fig. 5C, F, I, K, O), gas exchange uncertainty contributes more to total flux uncertainty than DO uncertainty during summer months. In the low-latitude regions (Fig. 5D, E, J, M, N), DO uncertainty generally dominates, especially where lower wind speeds yield consistent flux magnitudes across different gas exchange schemes. Over the ice-covered regions, wind product uncertainty also contributes substantially to total variance. At the hemispheric scale (Fig. 5S, T), fractional variance contributions resemble those at high latitudes, with gas exchange uncertainty dominating because high-latitude seasonal flux cycles drive hemispheric patterns.

https://doi.org/10.5194/essd-2025-738
Preprint. Discussion started: 23 December 2025

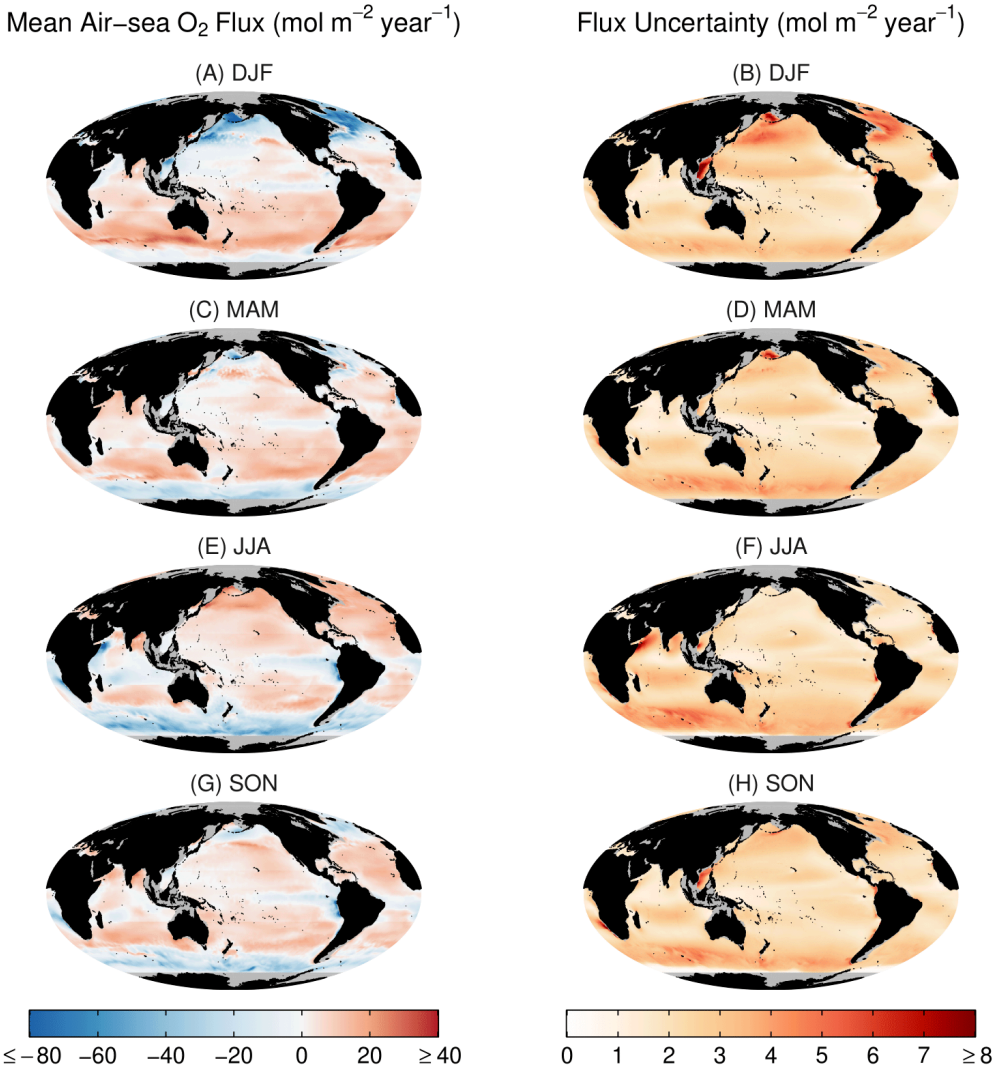

Fig. 1: Seasonal climatology of ensemble mean air-sea O_2 flux (left panels) and flux uncertainty (right panels) averaged over 2004-2024. Seasons shown are (A, B) December-January-February (DJF), (C, D) March-April-May (MAM), (E, F) June-July-August (JJA), and (G, H) September-October-November (SON). In the left column, positive values (red) indicate net ocean O_2 outgassing from the ocean. Uncertainty (right panels) represents one standard deviation (1-σ) of the seasonal flux climatology among the 9000 ensemble members. Gray areas indicate regions where data are unavailable in the GOBAI-O_2 v2.3 product. Monthly zonal average fluxes are shown in Fig. S2.

https://doi.org/10.5194/essd-2025-738
Preprint. Discussion started: 23 December 2025

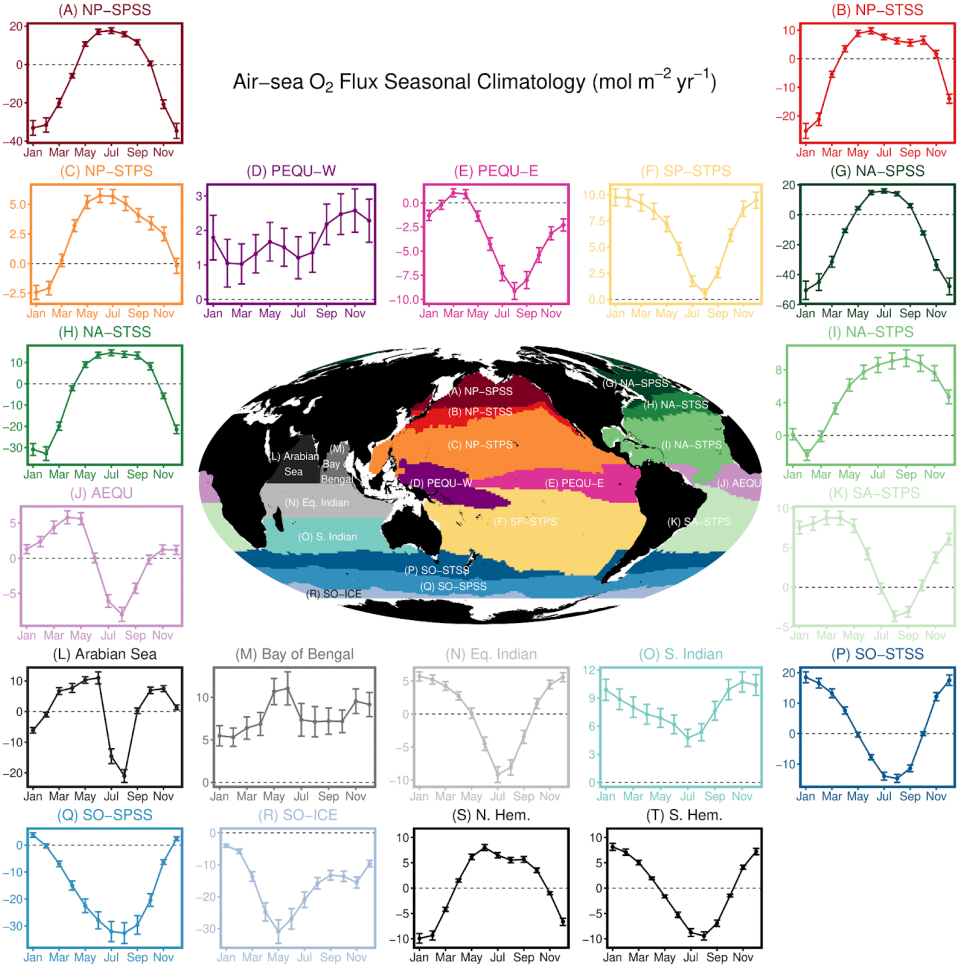

439

440 Fig. 2: Monthly climatology (2004-2024 average) of air-sea O_2 flux across 18 RECCAP2 regions
441 and for Northern and Southern Hemisphere averages. The region map is shown in the center,
442 with white areas indicating regions where DO data are unavailable in the GOBAI-O_2 v2.3
443 product. Panels are organized by ocean basins with Pacific regions from A to F, Atlantic regions
444 from G to K, Indian regions from L to O, Southern Ocean regions from P to R, and hemispheric
445 integrals in S and T. Panel titles and colors correspond to the region names and colors shown in
446 the center map. Y-axis ranges vary across panels to optimize visualization of seasonal flux
447 amplitude for each region. Error bars represent flux uncertainty estimated from the ensemble
448 standard deviation. Abbreviations include NP (North Pacific), SP (South Pacific), NA (North
449 Atlantic), SO (Southern Ocean), PEQU (Equatorial Pacific), AEQU (Equatorial Atlantic), SPSS
450 (subpolar seasonally-stratified), STSS (subtropical seasonally-stratified), STPS (subtropical
451 permanently-stratified), and ICE (seasonally ice-covered zone). We show interannual variability
452 of flux SCA in each region in Fig. S3. We compare the flux seasonal cycle with results from two
453 earlier versions of GOBAI-O_2 in Fig. S4, which shows generally good agreement but notable
454 differences in the Indian Ocean and subtropical oceans.

https://doi.org/10.5194/essd-2025-738
Preprint. Discussion started: 23 December 2025

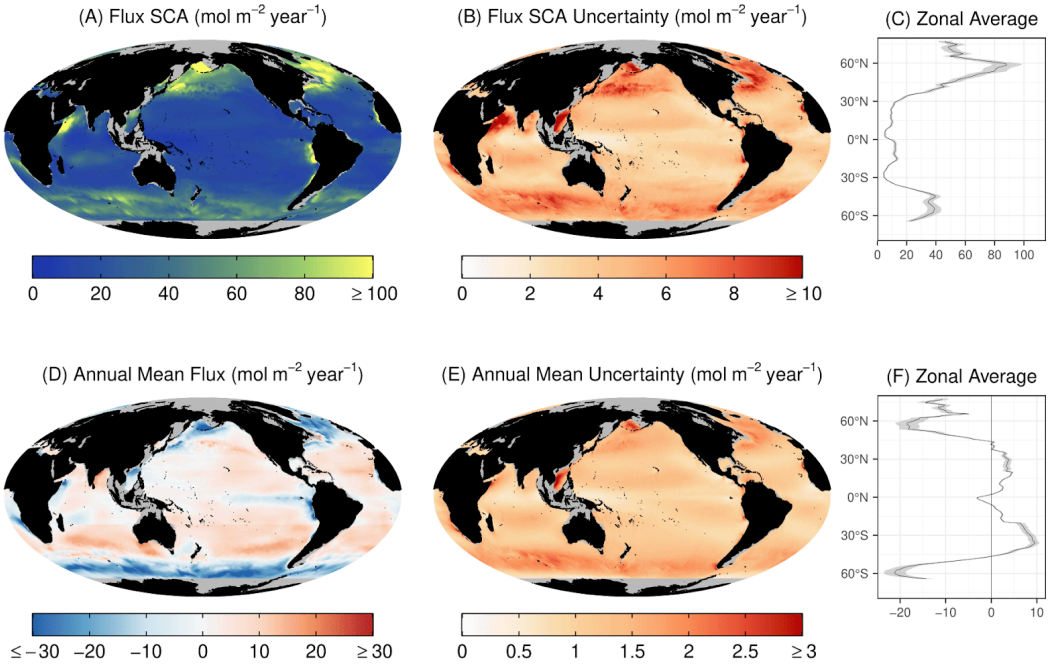

Fig. 3: Air-sea O_2 flux seasonal cycle amplitudes (SCA, A-C) and annual means (D-F). Gridded SCA (A) is calculated by first fitting a 2-harmonic function to the climatological monthly data (2004-2024), then calculating the difference between the seasonal maximum and minimum. The corresponding uncertainty (B) is calculated by applying this procedure to each ensemble member and then calculating the standard deviation. Gridded annual mean flux (D) represents the time average of all monthly fluxes, with uncertainty (E) calculated as the ensemble standard deviation. Zonal average SCA (C) and annual means (F) are calculated by first computing zonal and annual averages of monthly fluxes for each ensemble member, then fitting the 2-harmonic function (for SCA) or time-averaging (for annual mean). Gray shading in (C) and (F) represents uncertainty as the ensemble standard deviation across members.

https://doi.org/10.5194/essd-2025-738
Preprint. Discussion started: 23 December 2025

3.1.2 Flux annual mean

The zonal mean annual flux pattern suggests that the ocean is a strong annual O_2 sink at high latitudes, a weak sink at the equator, and a weak source in the subtropics (Fig. 3F). At the hemispheric scale, the Northern Hemisphere acts as a net annual O_2 source to the atmosphere (0.5±0.10 mol m^{-2} yr^{-1}) while the Southern Hemisphere is a net sink (-0.1±0.07 mol m^{-2} yr^{-1}), as shown in Figs. 4S and T, and Table 1. Over high-latitude regions, the Southern Ocean ice-covered zone is the strongest regional O_2 sink per area (-16.3± 1.78 mol m^{-2} yr^{-1}, Fig. 4R), followed by the subpolar Southern Ocean (-15.7± 1.77 mol m^{-2} yr^{-1}, Fig. 4Q) and the subpolar North Atlantic (-14.6±1.74 mol m^{-2} yr^{-1}, Fig. 4G). These regions experience vigorous deep-water formation driven by winter cooling, which increases O_2 solubility in cold surface waters and drives convective mixing that efficiently transfers O_2 to depth (Koelling et al., 2022). In addition, the upwelling of biologically O_2-depleted deep waters in these regions creates surface DO undersaturation that enhances atmospheric O_2 uptake (Boyer et al., 1999). The subpolar North Pacific exhibits a weaker sink (-6.0±0.90 mol m^{-2} yr^{-1}, Fig. 4A) than the North Atlantic, likely due to less vigorous deep convection and different circulation patterns.

Across equatorial regions, the Eastern Equatorial Pacific (-3.4±0.36 mol m^{-2} yr^{-1}, Fig. 4E) is a weak O_2 sink, while the other equatorial regions are O_2 sources, including the Western Equatorial Pacific (1.7±0.29 mol m^{-2} yr^{-1}, Fig. 4D), the Equatorial Atlantic (0.3±0.18 mol m^{-2} yr^{-1}, Fig. 4J), the Bay of Bengal (7.8±0.69 mol m^{-2} yr^{-1}, Fig. 4M) and the Equatorial Indian Ocean (0.3±0.36 mol m^{-2} yr^{-1}, Fig. 4N). The Eastern Equatorial Pacific experiences strong upwelling of O_2-depleted deep water from the oxygen minimum zone below, creating intense surface DO undersaturation that drives atmospheric O_2 uptake. The Equatorial Atlantic also experiences upwelling of O_2-depleted water, but this uptake is offset by stronger biological productivity that produces O_2, resulting in weak outgassing (Brandt et al., 2023). In contrast, the Western Equatorial Pacific is characterized by strong stratification that limits upwelling and receives O_2-rich water from the subtropical gyre, leading to surface DO supersaturation and net O_2 outgassing (Busecke et al., 2022; Fine et al., 1994).

The annual mean flux correction through DO adjustment (Appendix B) reduces O_2 outgassing in both hemispheres. Without adjustment, the raw flux calculation yields a global net O_2 outgassing

https://doi.org/10.5194/essd-2025-738
Preprint. Discussion started: 23 December 2025

of 1029 Tmol yr^{-1}, significantly larger than our observational constraint of an average of 61 Tmol yr^{-1}. This correction also reduces hemispheric flux asymmetry from 4.1 to 0.6 mol m^{-2} yr^{-1} by scaling down Northern Hemisphere annual flux from 5.7 to 0.5 mol m^{-2} yr^{-1} and Southern Hemisphere annual flux from 1.6 to -0.1 mol m^{-2} yr^{-1} (Fig. 4S and T, and Table 1). At the regional scale (Fig. 4), the correction reduces O_2 outgassing or increases O_2 uptake in all RECCAP2 regions except the Southern Ocean subpolar (Fig. 4Q) and ice-covered zone (Fig. 4R), where uptake decreases slightly from -15.7 to -15.1 and from -16.3 to -15.9 mol m^{-1} yr^{-1}, respectively.

Analysis of fractional variance contributions reveals distinct patterns in annual mean flux uncertainty across spatial scales (Fig. 5). At the hemispheric scale, uncertainty in annual mean flux for both the Northern and Southern Hemispheres is dominated by interactions among DO uncertainty, gas exchange parameterization, and wind products (Fig. 5S and T). At the regional scale, gas exchange parameterization dominates uncertainty in the subpolar regions, the subtropical regions, the Bay of Bengal, and the Equatorial Pacific. In contrast, DO uncertainty dominates flux uncertainty in the Equatorial Atlantic, and the Arabian Sea. The Equatorial Indian Ocean exhibits a unique pattern where wind uncertainty dominates, likely reflecting the strong influence of monsoon-driven wind variability during the northern summer.

https://doi.org/10.5194/essd-2025-738
Preprint. Discussion started: 23 December 2025

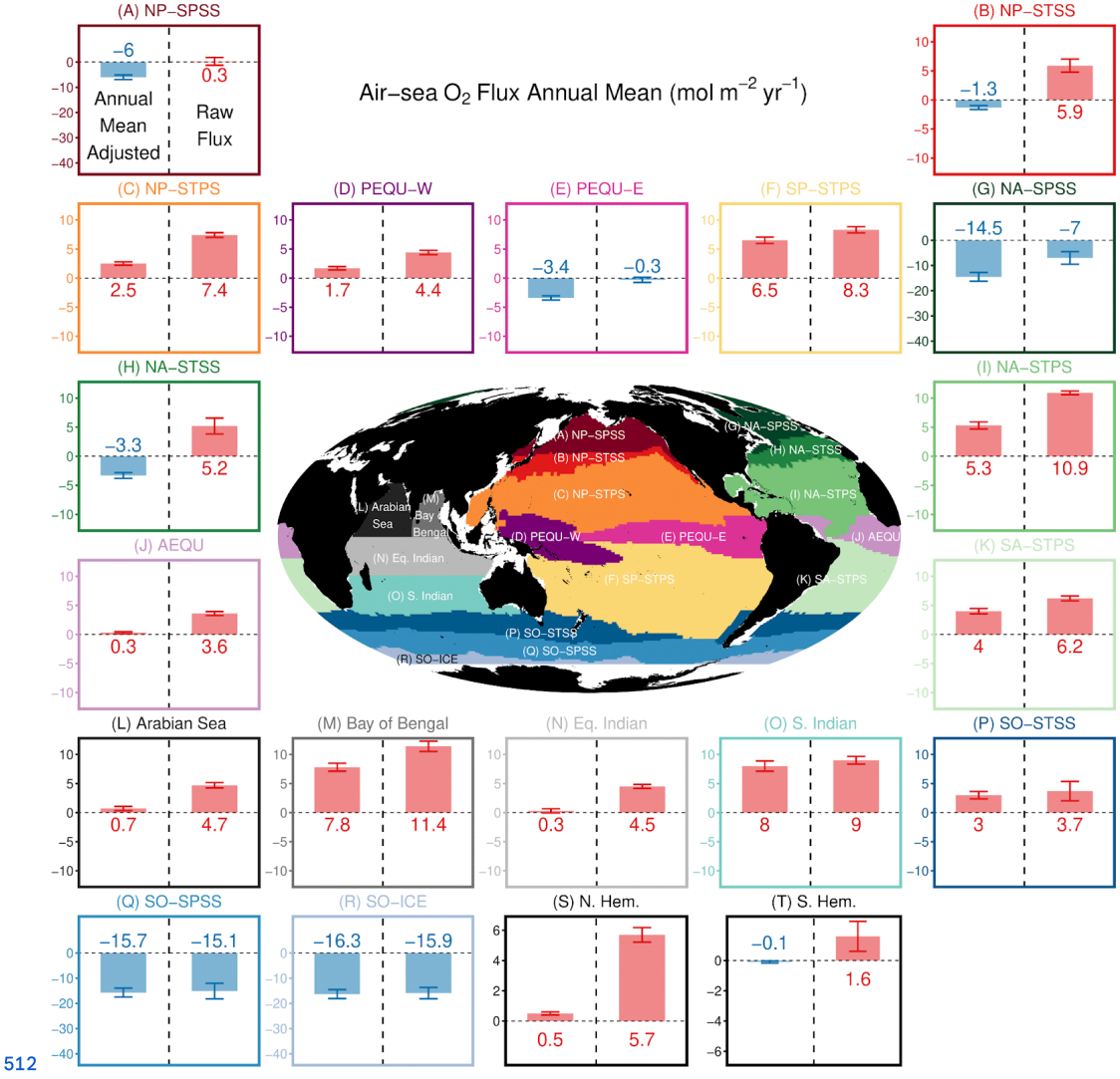

512

513 Fig. 4: Air-sea O_2 flux annual mean values for 18 RECCAP2 regions and Northern and Southern
514 Hemisphere averages. For each region, adjusted annual means (left in each panel) are compared
515 with raw flux estimates (right in each panel). Red bars have positive values that indicate net O_2
516 outgassing from the ocean, while blue bars have negative values that indicate net O_2 uptake.
517 Error bars represent the standard deviation across the flux ensemble. Ensemble average annual
518 mean flux values are labeled for each estimate and are also reported in Table 1 with 1-σ
519 uncertainties. Y-axis ranges for the four high-latitude regions (Panels A, G, Q, and R) and
520 hemispheric averages (Panels S and T) differ from those in other panels to optimize visualization
521 of their distinct flux magnitudes. We compare the annual mean flux resolved using two earlier
522 versions of GOBAI-O_2 in Fig. S5.

https://doi.org/10.5194/essd-2025-738
Preprint. Discussion started: 23 December 2025

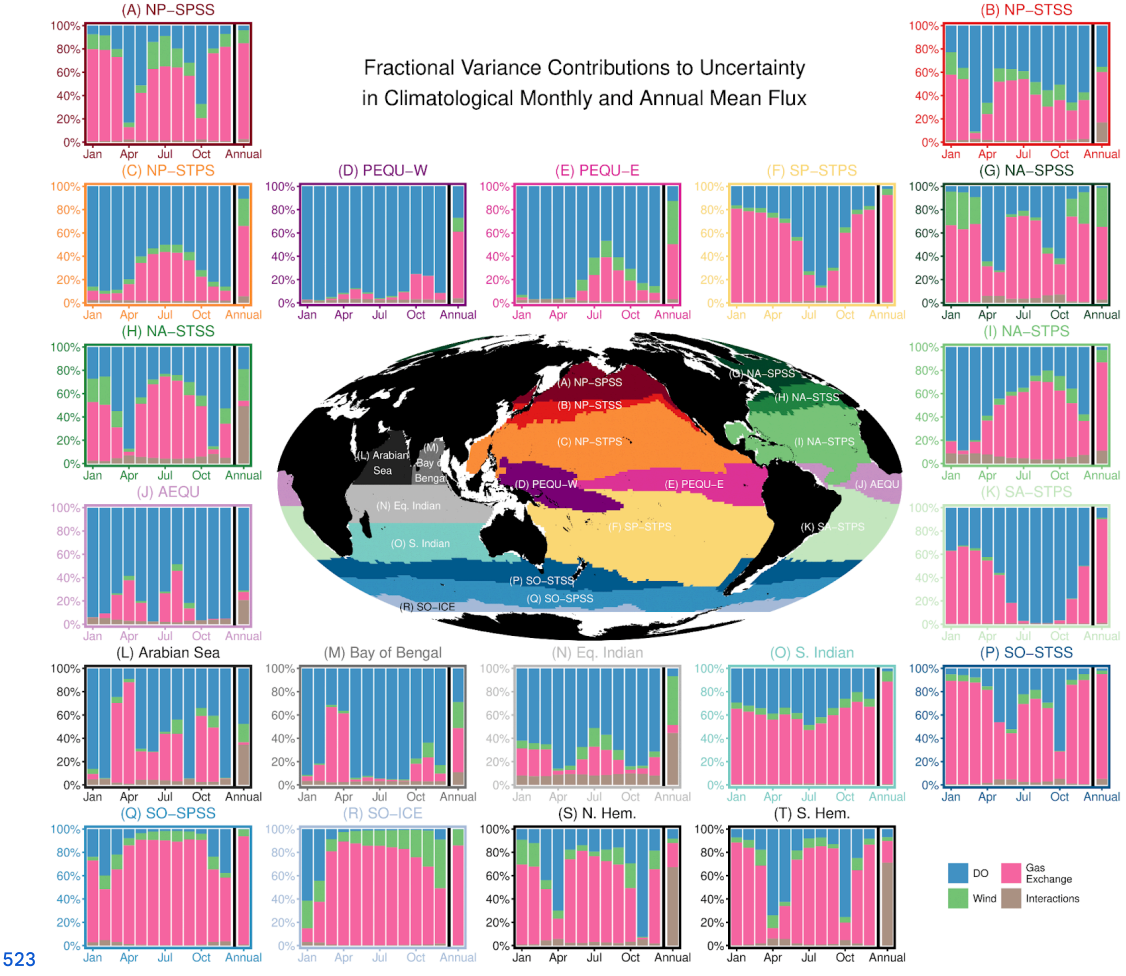

Fig. 5: Fractional variance contributions to uncertainty in climatological monthly and annual mean O_2 flux across global ocean regions. Stacked bar charts show the relative contributions of different uncertainty sources for each month (2004-2024 climatology) and for the annual mean (rightmost bar, 2004-2024 average). Uncertainty sources include variability in DO fields from 1000 ensemble members with annual mean adjustment (blue), three wind products (green), three gas exchange parameterizations schemes (pink), and the combined interactions between these three factors (brown). Variance fractional contributions are estimated using a three-way factorial mixed-effects analysis of variance (ANOVA) with the REML package in R (Bates et al., 2015).

https://doi.org/10.5194/essd-2025-738
Preprint. Discussion started: 23 December 2025

532 Table 1: SCA and annual mean values of air-sea O_2 flux for 18 RECCAP2 regions and the
533 Northern and Southern Hemispheres. SCA is calculated by first fitting a 2-harmonic function to
534 the climatological monthly data (2004-2024 average), then calculating the difference between the
535 seasonal maximum and minimum. Region acronyms are defined in Fig. 2.

Regions	SCA		Annual Mean	
	mol m^{-2} yr^{-1}	Tmol yr^{-1}	mol m^{-2} yr^{-1}	Tmol yr^{-1}
(A) NP-SPSS	56.2 ± 5.35	646 ± 61.4	-6.0 ± 0.90	-68 ± 10.3
(B) NP-STSS	34.7 ± 3.26	247 ± 23.2	-1.3 ± 0.33	-9 ± 2.3
(C) NP-STPS	8.4 ± 0.79	351 ± 32.7	2.6 ± 0.29	107 ± 12.2
(D) PEQU-W	1.9 ± 0.58	21 ± 6.4	1.7 ± 0.29	19 ± 3.2
(E) PEQU-E	10.0 ± 0.86	152 ± 13.0	-3.4 ± 0.36	-52 ± 5.5
(F) SP-STPS	9.1 ± 0.70	491 ± 37.8	6.5 ± 0.55	351 ± 29.7
(G) NA-SPSS	70.0 ± 7.44	486 ± 51.6	-14.6 ± 1.74	-101 ± 12.1
(H) NA-STSS	48.3 ± 4.02	286 ± 23.8	-3.3 ± 0.49	-19 ± 2.9
(I) NA-STPS	11.2 ± 0.97	244 ± 21.2	5.3 ± 0.61	115 ± 13.3
(J) AEQU	14.2 ± 1.60	118 ± 13.3	0.3 ± 0.18	2 ± 1.5
(K) SA-STPS	12.8 ± 0.92	244 ± 17.6	4.0 ± 0.46	76 ± 8.8
(L) Arabian sea	29.4 ± 2.80	199 ± 18.9	0.7 ± 0.37	5 ± 2.5
(M) Bay of Bengal	6.1 ± 1.52	21 ± 5.2	7.8 ± 0.69	27 ± 2.4
(N) Eq. Indian	14.7 ± 1.34	227 ± 20.8	0.3 ± 0.36	5 ± 5.6
(O) S. Indian	6.0 ± 0.67	101 ± 11.3	8.0 ± 0.89	134 ± 15.0
(P) SO-STSS	35.2 ± 3.00	984 ± 83.8	3.0 ± 0.64	85 ± 17.9
(Q) SO-SPSS	38.2 ± 4.56	1156 ± 138.1	-15.7 ± 1.77	-476 ± 53.6
(R) SO-ICE	26.6 ± 3.44	234 ± 30.4	-16.3 ± 1.78	-144 ± 15.6
(S) N. Hem.	17.7 ± 1.48	2257 ± 187.2	0.5±0.10	67 ± 12.6
(T) S. Hem.	17.9 ± 1.48	3385 ± 280.2	-0.1±0.07	-6 ± 13.3

https://doi.org/10.5194/essd-2025-738
Preprint. Discussion started: 23 December 2025

3.2 Flux evaluation

3.2.1 Flux seasonal cycle

We compare 2-harmonic fits of latitudinally-binned airborne tropospheric-average ΔO_2^{ocn} from TM3 forward transport simulation of ensemble mean fluxes with airborne ΔO_2^{ocn} observations fitted in the same way (Fig. 6). The simulations and observations show good overall agreement. In the northern mid-to-high latitudes (60°–80°N), our simulations successfully capture the prolonged outgassing period and the double-peak structure observed in atmospheric data (Fig. 6), and agree with the observed SCA (Table 2). In the southern mid-to-high latitudes (40°–80°S), our simulations underestimate the SCA by 10%, primarily due to a weak summertime peak. In the low latitudes (20°S–20°N), our simulations generally overestimate SCA by up to 30%, though this represents a small absolute bias given the weak seasonal cycles in these regions. In the high latitudes of both hemispheres, our simulations lag the observed seasonal peaks by about a month, suggesting that peak outgassing occurs too late in the flux product. Simulated seasonal trough timing generally lags observations by one to three weeks, except in the mid-latitude Southern Hemisphere (40°–20°S), where the phase lag is much larger, reaching six weeks. The mechanisms driving these phase lags remain unclear and require further investigation. RMSE (Table 2) is higher in the Southern Hemisphere than in the Northern Hemisphere. The largest RMSE occurs at high southern latitudes (9 per meg), which remains much smaller than the seasonal amplitude (73 per meg).

Our hemispheric-scale seasonal flux cycles improve on the widely used GK01 flux product (Garcia and Keeling, 2001), as shown in Fig. S6. GK01 significantly underestimates the flux seasonal cycle at high latitudes in both hemispheres and fails to resolve the prolonged summer outgassing in the northern mid to high latitudes with distinct double-peak structure from 40°–60° N. These complex seasonal characteristics in the Northern Hemisphere have been independently confirmed by hemispheric flux estimates derived from atmospheric measurements at both surface stations and from airborne surveys (Jin et al., 2023; Rödenbeck et al., 2008). These patterns are also seen in one configuration of the Community Earth System Model (Yeager et al., 2022). While the simulated seasonal cycle in our flux product generally lags in phase relative to the airborne observations, the simulated seasonal cycle in GK01 leads the observations by 1-2

https://doi.org/10.5194/essd-2025-738
Preprint. Discussion started: 23 December 2025

565 weeks at mid to high latitudes in the Southern Hemisphere. This phase difference likely reflects
566 the methodological assumption in GK01 that ocean heat flux and O_2 flux are in phase.

567 Forward transport of the ensemble mean flux resolved using each gas exchange parameterization
568 and CCMP winds shows that the L13 scheme produces the smallest simulated ΔO_2^{ocn} SCA,
569 while the W97 scheme produces the largest ΔO_2^{ocn} SCA (Fig. S7), consistent with the order of
570 flux SCA resolved using these three schemes (Fig. A1). A similar test using each of the three
571 wind products with the L13 scheme yields consistent SCA (Fig. S8). Using these airborne data to
572 evaluate the three gas exchange parameterizations and three wind products is complicated by
573 potential biases in DO fields.

574 It is important to note that, while we use only one transport model, our results are not biased by
575 potential uncertainties in forward transport simulations. Using tropospheric-average atmospheric
576 concentrations as the evaluation metric effectively eliminates potential biases from transport
577 model representations of vertical mixing. An earlier study of Jin et al. (2025) demonstrated that
578 different transport models are highly consistent in simulating tropospheric-average airborne APO
579 but show significant spread at surface stations. Nevertheless, we show that at most surface
580 stations (Fig. S9), model simulations still agree with observations in seasonal amplitude and
581 phase, though consistent phase lags are evident, similar to those observed in the airborne data
582 comparison (Fig. 6). The largest biases occur at LJO and CBA (Fig. S9), both eastern Pacific
583 coastal sites, likely due to vertical mixing and coastal wind biases in the TM3 model, as reported
584 by an earlier study (Jin et al., 2025).

https://doi.org/10.5194/essd-2025-738
Preprint. Discussion started: 23 December 2025

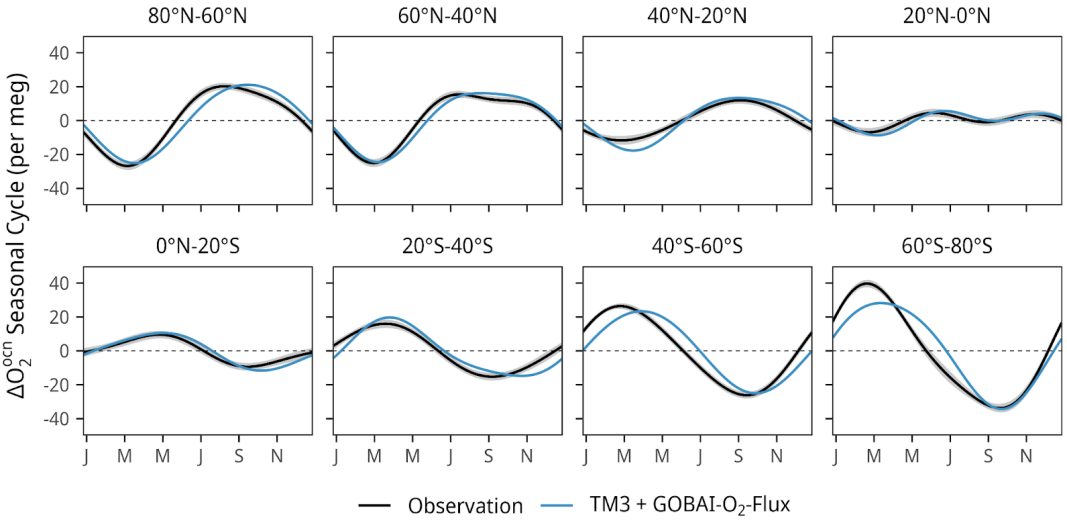

585

586 Fig. 6: Comparison of tropospheric-average (1000 to 400 mbar) seasonal atmospheric ΔO_2^{ocn}
587 between observations and simulations for eight latitude bands from 80°N to 80°S. Observations
588 (black) are derived from airborne APO data corrected for non-oceanic O_2 flux components
589 (Appendix C). Model simulations are based on TM3 forward transport of our flux estimates
590 (GOBAI-O_2-Flux). The transport model simulations provide co-samplings at each observation
591 time and location, ensuring direct comparison without spatial and temporal sampling bias.
592 Airborne observations and model simulations are first detrended using observed or simulated
593 surface station trends. These surface station trends are determined by linear fits to
594 multiple-station weighted averages following Hamme and Keeling (2008). The detrended
595 airborne observations and model simulations between 1000–400 mbar are then binned by latitude
596 band. Stratospheric data are filtered out based on airborne measurements of water vapor, O_3, and
597 N_2O (Section 2.7). For each latitude band, the seasonal cycle is calculated by applying a
598 2-harmonic fit to the detrended data after removing the annual mean. Gray shading represents
599 uncertainty in the observed seasonal cycle, combining measurement uncertainty and uncertainty
600 in atmospheric non-oceanic O_2 component corrections estimated from an ensemble of flux
601 products and transport models (Appendix C). For each latitude band, Table 2 reports the root
602 mean square error (RMSE), phase lag based on the seasonal peak and trough, and SCA ratio
603 (simulated/observed). A comparison with TM3 forward transport of the GK01 (Garcia and
604 Keeling, 2001) air-sea O_2 flux product is shown in Fig. S6.

https://doi.org/10.5194/essd-2025-738
Preprint. Discussion started: 23 December 2025

Table 2: Performance metrics comparing simulated and observed ΔO_2^{ocn} seasonal cycles across eight latitude bands. RMSE (per meg), phase lag (days), and SCA ratios are shown. Positive phase lags indicate that the simulated seasonal cycle lags behind observations. SCA ratio is calculated as simulated SCA divided by observed SCA.

Latitude band	RMSE (per meg)	SCA ratio	Peak lag (days)	Trough lag (days)
80-60°N	5.1	1.0	37	11
60-40°N	3.0	1.0	33	7
40-20°N	3.7	1.3	-3	19
20-0°N	1.8	1.3	17	14
0-20°S	2.2	1.2	6	21
20-40°S	4.3	1.1	7	46
40-60°S	7.5	1.0	34	15
60-80°S	9.0	0.9	22	3

https://doi.org/10.5194/essd-2025-738
Preprint. Discussion started: 23 December 2025

3.2.2 Annual mean flux

We use long-term trends in ΔO_2^{ocn} at surface stations, isolated from APO measurements by correcting other components (Eq. C1), to evaluate global annual mean air-sea O_2 fluxes. As shown in Fig. 7, the observed APO is decreasing at a rate of −11.6 ± 0.44 per meg year^{-1}. This decline is driven by multiple components, including air-sea CO_2 flux, air-sea N_2 flux, and fossil fuel burning, all of which contribute negatively to the APO trend. The residual ΔO_2^{ocn} shows a small but highly uncertain increase of 1.4 ± 1.12 per meg year^{-1}, suggesting a net global ocean O_2 outgassing. The trend in annual mean ΔO_2^{ocn} (reported in Fig. 7) thus serves as a metric for evaluating global annual mean O_2 flux estimates. Our forward transport simulation, with annual mean flux adjustments derived from ocean heat fluxes, produces a trend of 1.5 ± 0.80 per meg year^{-1}, in agreement with the observation-based estimate. In contrast, the forward transport simulation using raw fluxes yields a substantially larger trend of 27.5 ± 4.67 per meg year^{-1}, significantly overestimating the observed ΔO_2^{ocn} trend and highlighting the importance of the annual mean flux adjustment.

We use airborne observations of tropospheric-mean annual-mean ΔO_2^{ocn} for eight latitude bands spanning 80°S to 80°N to evaluate the meridional gradient of annual mean O_2 fluxes (Fig. 8). In the Northern Hemisphere, the meridional gradient is larger in simulations (~-0.14 per meg lat^{-1}, positive northward) than in observations (-0.07±0.01 per meg lat^{-1}). This overestimation is largely due to the absence of an observed rebound at 60°N–80°N in the simulations. In the Southern Hemisphere, the simulated meridional gradient (0.20 per meg lat^{-1}) is much larger than the observed gradient (0.04±0.02 per meg lat^{-1}). These biases in both hemispheres produce an overly strong simulated “equatorial bulge” and annual mean ΔO_2^{ocn} values that are too low, relative to the global mean, at high southern latitudes.

Biases in the annual mean meridional gradients indicate that regional annual mean flux constraints from the ocean inversions (Resplandy et al., 2016) overestimate either or both O_2 outgassing in the equatorial region and O_2 uptake at high southern latitudes. Nevertheless, applying these constraints improves flux estimates by reducing the meridional flux gradient, particularly in the Southern Hemisphere, from 0.32 to 0.20 per meg lat^{-1} (not shown). Specifically, the adjustment reduces equatorial outgassing by lowering the annual mean DO (Fig.

https://doi.org/10.5194/essd-2025-738
Preprint. Discussion started: 23 December 2025

639 B2). Earlier studies highlighted similar strong flux “tropical bulges” evident in other ocean
640 inversion products (Battle et al., 2006; Gruber et al., 2001), and in prognostic ocean
641 biogeochemistry models (Stephens et al., 1998). However, previous observational studies do not
642 support this bulge, or only show a small bulge (Pickers et al., 2017; Stephens et al., 1998;
643 Tohjima et al., 2012). The airborne observations shown in Fig. 8 similarly preclude a large
644 equatorial bulge, showing only a small (~3 per meg) enhancement from 0°–20°S relative to
645 60°–80°S.

https://doi.org/10.5194/essd-2025-738
Preprint. Discussion started: 23 December 2025

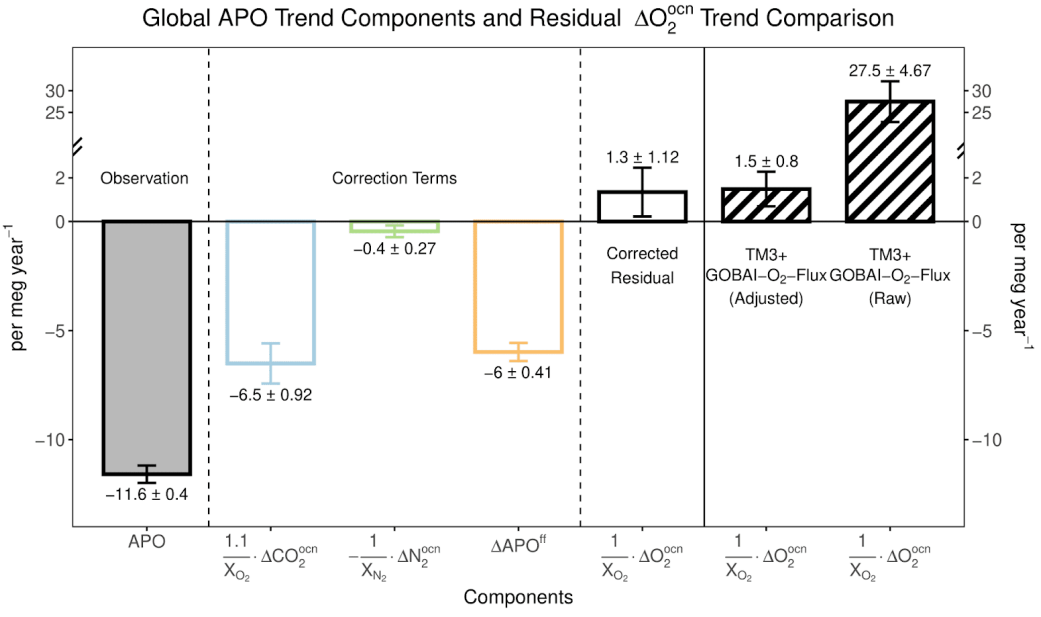

646

647 Fig. 7: Global station-average annual mean APO trend, components that contribute to APO
648 trend, the residual ΔO_2^{ocn}, and comparison to TM3 + GOBAI-O_2-Flux model simulations of
649 ΔO_2^{ocn}. Annual mean values of APO and components are calculated as a weighted average of
650 data from seven surface sampling sites across the Pacific basin within the Scripps O_2 program
651 (Keeling, 2019), with weights following Hamme and Keeling (2008). Correction terms are each
652 flux component forward transported by four atmospheric transport models and sampled at station
653 locations and flask collection times, available from Jin et al., (2025), and further scaled to
654 represent its contributions to the APO trend, following Eq. C1. Trend is calculated as a linear fit
655 to data from 2005 to 2020. Uncertainty in APO trend is calculated from the station $\delta(O_2/N_2)$ error
656 model (Appendix C). Uncertainty in three correction terms are based on the simulated trend
657 calculated using two different flux components and four transport models (8 combinations).
658 Uncertainty in TM3 + GOBAI-O_2-Flux simulations are scaled by the uncertainty in annual mean
659 fluxes averaged over 2005 to 2020 divided by the ensemble mean annual flux.

https://doi.org/10.5194/essd-2025-738
Preprint. Discussion started: 23 December 2025

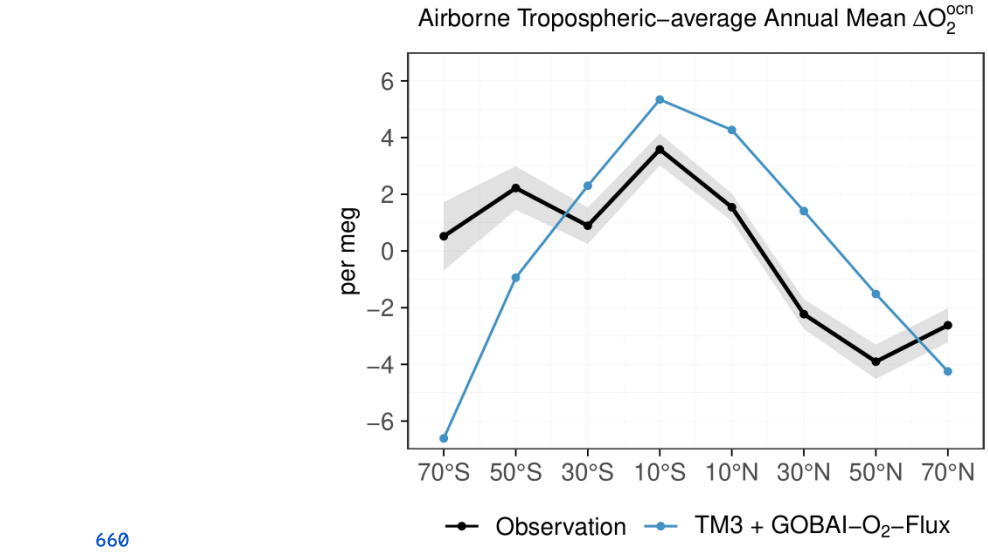

Fig. 8: Comparison of the meridional gradient in airborne tropospheric-average annual mean ΔO_2^{ocn} between observations (black) and TM3 + GOBAI-O_2-Flux simulations (blue) for eight latitude bands spanning 80°N to 80°S at 20° intervals. Data processing, including detrending, binning, and filtering, follows the same procedure described in the Fig. 6 caption. For each latitude band, the annual mean value is calculated by applying a two-harmonic fit with constant offset to the detrended data, and using the offset to represent the annual mean value. The global mean, averaged across all eight latitude bands, is subtracted to center the global annual mean in both lines at 0. Because model simulations have arbitrary global mean values before this subtraction, only the meridional gradient of the annual mean values should be interpreted, rather than the absolute values. Gray shading represents uncertainty in the observed annual mean values, combining measurement uncertainty and uncertainty in the atmospheric non-oceanic O_2 component corrections estimated from an ensemble of flux products and transport models (Appendix C).

4 Caveats and future direction

4.1 Data gaps

Our flux calculations are limited by spatial data gaps in GOBAI-O_2 DO fields. We could not resolve flux estimates over the Arctic (north of 79.5°N), parts of the Southern Ocean seasonally ice-covered zone (south of 64.5°S), and most coastal regions due to these regions not being included in the GOBAI-O_2 products. These regions account for approximately 18% of Northern Hemisphere oceans and 8% of Southern Hemisphere oceans, collectively representing 14% of

https://doi.org/10.5194/essd-2025-738
Preprint. Discussion started: 23 December 2025

the global ocean area. Simple area scaling has been used to correct pCO_2 products for similar issues (Friedlingstein et al., 2025), but is limited by these regions likely having unique fluxes.

High-latitude polar regions exhibit distinct seasonal variations in physical and biogeochemical processes due to extreme light and temperature cycles, suggesting large seasonal cycles in air-sea O_2 flux. Atmospheric O_2 observations collected at surface stations and along ship transects confirm significant seasonal variation in these regions (Ishidoya et al., 2016; Jin et al., 2025; Keeling et al., 2020; Stephens, 2025). The absence of flux estimates from these polar regions likely leads to underestimation of the true seasonal amplitude in regional to hemispheric seasonal flux cycles. TM3 forward transport simulations indicate that flux SCA in the high southern latitudes is underestimated (Fig. 6), likely influenced by the lack of GOBAI-O_2 data south of 64.5°S, where summertime blooms could be underrepresented.

Similarly, the absence of coastal data limits our representation of nearshore processes that exhibit intense seasonal biogeochemical activity due to coastal upwelling and riverine nutrient inputs. Satellite-based chlorophyll-a data reveal significant blooms in coastal regions, for example, east of the South American coast (Behrenfeld et al., 2005). Without O_2 flux estimates over these regions, we potentially miss summer-time O_2 outgassing events associated with high biological productivity.

Here we explore the contribution of these data gaps to area-integrated flux seasonal cycles in the Northern Hemisphere and Southern Hemisphere using a Community Earth System Model version 2 (CESM2) Forced Ocean-Sea-Ice (FOSI) simulation (Yeager et al., 2022), which was evaluated as providing a reasonably good global air-sea O_2 flux (Jin et al., 2023, 2025). By excluding GOBAI-O_2 data-gap grid cells from the CESM2 output, the 2011-2020 average seasonal flux amplitude is reduced from 14.9 to 14.2 mol m^{-2} $year^{-1}$, and from 16.1 to 15.1 mol m^{-2} $year^{-1}$ in the Northern and Southern Hemisphere, respectively.

Spatial data gaps also introduce uncertainties in annual mean flux estimates. We assume zero flux and zero annual DO adjustment over these gaps. This ensures that extratopical annual mean fluxes match the ocean-inversion constraints. However, this assumption may spatially bias regional estimates by assigning compensatory fluxes to resolved areas. We also explore the contribution of these data gaps to area-integrated annual mean fluxes in the equatorial region

https://doi.org/10.5194/essd-2025-738
Preprint. Discussion started: 23 December 2025

(20°S-20°N), northern extratropics (>20°N), and southern extratropics (<20°S) using CESM. The 2011-2020 average equatorial outgassing decreases from 214 to 191 Tmol, northern extratropical ingassing increases from 55 to 56 Tmol, and southern extratropical ingassing decreases from 45 to 37 Tmol. This calculation indicates that our zero-flux assumption overestimates tropical outgassing and southern ingassing in resolved regions to compensate for missing fluxes.

4.2 DO machine-learning interpolation methods

Our flux estimates might be limited by potential systematic biases in GOBAI-O_2 DO fields arising from the ML methodology. Here we employ the latest GOBAI-O_2 version v2.3. Alternatively, we resolve fluxes using two earlier versions v2.1 and v2.2, which use slightly different ML methodologies (Section 2.1). While hemispheric-scale O_2 flux seasonal climatologies remain consistent across all three versions (Fig. S4), regional discrepancies emerge, especially over the Indian and equatorial regions, where sparse observations make reconstructed DO fields sensitive to methodological differences.

We find large deviations in uncorrected regional to global annual mean fluxes across three versions of GOBAI-O_2 (Fig. S5). While v2.3 suggests a 1029 Tmol yr^{-1} annual outgassing, v2.1 (2004-2022 average) indicates a net O_2 uptake of 707 Tmol yr^{-1} and v2.2 (2004-2023 average) shows a net O_2 uptake of 258 Tmol yr^{-1}. These strong O_2 uptake estimates in v2.1 and v2.2 result from a combination of stronger O_2 sinks in the Southern Hemisphere and weaker O_2 sources in the Northern Hemisphere compared to v2.3 (Fig. S5S and T), indicating that the annual flux is particularly sensitive to small perturbation in DO. The global annual flux from these two earlier versions also significantly deviates from our heat flux constraint of an average of 61 Tmol yr^{-1}. Although our heat flux constraint removes spread in global annual mean flux resolved across DO versions, large differences in regional annual mean flux persist even after adjustment (Fig. S5).

The DO method uncertainty in GOBAI-O_2 depends on the distribution of available training data and the ability of ML algorithms to represent underlying system variability, with larger uncertainties in regions of high natural variability and sparse sampling (Fig. 5). High uncertainties could also occur where water masses with similar physical characteristics but different oxygen signatures mix, highlighting challenges in distinguishing biogeochemical from

https://doi.org/10.5194/essd-2025-738
Preprint. Discussion started: 23 December 2025

physical drivers using available training parameters. While ML reconstructions provide spatially and temporally complete datasets, they may exhibit smoothing effects that dampen extreme surface ocean DO values critical for accurate flux estimates on short timescales. The monthly temporal resolution may also fail to resolve episodic events that significantly contribute to regional flux budgets. For example, ocean heat waves that lead to low oxygen extremes (Li et al., 2024), storm-induced deep mixing events that induce surface cooling and potentially draw-down of surface DO and also phytoplankton blooms afterwards (Walker et al., 2005), and episodic phytoplankton blooms induced by dust deposition over the Indian Ocean (Banerjee and Kumar, 2014). Furthermore, ML models are inherently limited by their training data, meaning poorly-represented processes or conditions may not be accurately captured in reconstructions.

GOBAI-O_2 integrates observations from both ship-based measurements and Argo floats, and therefore, offsets between these platforms and between ships could introduce systematic biases in reconstructions, requiring more careful strategies to synthesize these datasets (Bushinsky et al., 2025). The latest v2.3 has applied corrections to Argo measurements to minimize systematic biases.

We note that there are other gridded global ocean DO products available that could be used to calculate air-sea O_2 fluxes. Ito et al. (2024) provide monthly mean DO fields from 1965-2020 at 1°×1° resolution from Pole-to-Pole and from surface to 1000 m depth. This product uses neural networks and random forest regression to construct DO fields by relating historical data from ship-based measurements (bottle and CTD-O_2) and BGC-Argo profiles (after 2005) to climate, spatial, and temporal variables. Gouretski et al. (2024) provide monthly mean DO fields from 1960 onward at 1°×1° resolution from Pole-to-Pole and from surface to 6000 m depth. This product applies enhanced quality control procedures to data from bottle, CTD, and Argo float measurements, then uses a mapping method (Cheng et al., 2017) to spatially interpolate oxygen data. While these products offer valuable DO fields, we chose GOBAI-O_2 because it provides detailed, source-specific uncertainty estimates that facilitate quantifying flux uncertainty through large ensembles. Additionally, our goal is to illustrate the feasibility of calculating air-sea O_2 fluxes from ML-based DO products rather than to conduct a full intercomparison of different observational products. Nevertheless, future studies could focus on calculating fluxes using

https://doi.org/10.5194/essd-2025-738
Preprint. Discussion started: 23 December 2025

768 different products and quantifying differences in flux estimates arising from distinct
769 methodologies.

770 4.3 Gas exchange parameterization

771 Robust O_2 flux calculations through gas exchange parameterization require a better
772 understanding of bubble-mediated flux processes. An earlier study identified that in the Labrador
773 Sea, two-thirds of annual oxygen uptake occurs over only 40 days in winter due to
774 bubble-mediated air-sea gas transfer under high wind and deep convection conditions
775 (Atamanchuk et al., 2020). For individual regions, the ensemble mean flux calculated using each
776 gas exchange scheme shows significant uncertainty, especially over high-latitude regions in
777 winter, leading to large spread in annual mean flux estimates (Fig. A1). These wintertime flux
778 anomalies largely shape the seasonal flux cycle. Our flux seasonal cycle evaluation (Fig. 6)
779 reveals certain errors (i.e., RMSE) at high latitudes.

780 Recent advances in gas exchange theory offer promising improvements for future studies. The
781 universal wind-wave-bubble formulation developed by Deike et al. (2025) explicitly accounts for
782 asymmetric bubble-mediated fluxes through wave breaking statistics. This approach has
783 demonstrated improved representation of DO concentrations in Pacific Subantarctic Mode
784 Waters during their formation period in winter (August–September), suggesting it could
785 substantially reduce uncertainties in regional O_2 flux estimates, particularly in high-latitude
786 winter conditions where bubble processes dominate.

787 4.4 Annual mean flux

788 Our study shows the annual mean O_2 flux estimates remain the largest uncertainty. Reducing this
789 uncertainty is critical for using atmospheric O_2 and CO_2 observations to constrain land and ocean
790 carbon partitioning through budget equations (Bender et al., 2005; Friedlingstein et al., 2025;
791 Keeling and Manning, 2014). Future research should focus on resolving annual mean fluxes and
792 their interannual variability by improving ocean interior DO reconstructions and developing
793 independent constraints that capture interannual flux variations.

https://doi.org/10.5194/essd-2025-738
Preprint. Discussion started: 23 December 2025

5 Conclusion

We develop a gridded product of monthly open ocean air-sea O_2 flux from 2004 to 2024 on a 1°×1° grid, leveraging ML-based DO data products (GOBAI-O_2), combined with three gas exchange parameterization schemes and three wind products. By incorporating a large ensemble approach to quantify uncertainties and applying regional adjustments to align annual mean fluxes with those derived from scaling ocean heat flux and from ocean inversions, our product provides a robust representation of air-sea O_2 fluxes. This dataset captures pronounced seasonal variability across latitude as well as the global annual mean flux. However, the meridional annual mean flux pattern is biased toward excessive ingassing in the high southern latitudes and too large outgassing in the equatorial region. Our results also reveal distinct basin-scale differences in both flux patterns and seasonal amplitudes.

At the hemispheric scale, our flux estimates reveal the expected seasonal pattern of net oceanic outgassing during summer and net uptake during winter, driven by the combined effects of thermal solubility changes and seasonal biological productivity cycles (Figs. 1-3). Significant asymmetries exist between hemispheres, with the Northern Hemisphere exhibiting prolonged summer outgassing periods lasting seven months and characteristic double-peak structures that reflect complex interactions between mixed-layer changes and biological productivity. Regional flux analysis reveals strong flux seasonal variations in subpolar regions, with the North Atlantic subpolar zone and the high-latitude SO showing the most intense flux amplitudes due to deep-water formation (Bushinsky et al., 2017; Koelling et al., 2022; Silva et al., 2024) and extreme thermal cycling. Our global annual mean constraint forces the global ocean to be a weak source of O_2 (Figs. 3-4). On the regional scale, strong sinks dominate at high latitudes where cold water formation and upwelling of oxygen-depleted deep waters create persistent undersaturation, while weak sinks characterize equatorial upwelling zones where oxygen-poor waters reach the surface (Eddebbar et al., 2017). In contrast, weak sources occur in subtropical gyres and near the Equator (e.g., 5° to 20°) where warm, stratified conditions and biological productivity combine to create surface supersaturation and net outgassing to the atmosphere.

Our uncertainty analysis reveals distinct patterns in the dominant sources of flux uncertainty that vary by both geographic region and temporal scale (Fig. 5). For monthly climatological fluxes,

https://doi.org/10.5194/essd-2025-738
Preprint. Discussion started: 23 December 2025

823 gas exchange uncertainty dominates at high latitudes due to the large spread in bubble-mediated
824 flux estimates under high wind conditions, where different parameterization schemes show
825 substantial disagreement in their representation of air injection processes. In contrast, DO
826 uncertainty controls flux uncertainty in low-latitude regions, particularly in areas with sparse
827 observational coverage where ML reconstruction methods struggle to accurately represent the
828 true spatial and temporal variability of ocean biogeochemistry. The annual mean flux uncertainty
829 follows similar geographic patterns for individual regions, but at the hemispheric scale becomes
830 dominated by complex interactions between DO, gas exchange parameterization, and wind
831 uncertainties. We note that uncertainty due to DO may essentially stem from the annual mean
832 flux adjustment that corrects DO concentrations for each ensemble member.

833 We evaluate our flux estimates by comparing forward transport simulations with global
834 atmospheric O_2 observations that have been corrected for non-oceanic O_2 flux contributions
835 (Figs. 6-8). For seasonal cycles, our results show good agreement with airborne
836 tropospheric-average ΔO_2^{ocn} observations, though we find systematic overestimation of SCA at
837 low latitudes and underestimation of SCA at high southern latitudes (Fig. 6 and Table 2). We also
838 find that seasonal maximum timing lags observations by about a month in high latitudes of both
839 hemispheres, and the seasonal minimum timing lags observations across all latitudes, with
840 particularly large lags of six weeks in southern low latitudes (40° - 20°S). On annual mean
841 timescales, the agreement between simulated and observed long-term atmospheric ΔO_2^{ocn} trend
842 supports the reasonableness of our constrained global annual mean flux of an average of 61 Tmol
843 yr^{-1} (Fig. 7). However, this observational constraint has large uncertainty due to its sensitivity to
844 the other components used to isolate ΔO_2^{ocn} from APO measurements (Fig. 7). Meridional
845 gradients in annual mean atmospheric concentrations reveal regional biases, with simulations
846 showing excessive ΔO_2^{ocn} in tropical regions relative to high latitudes, suggesting overestimated
847 extratropical ocean uptake and overestimated tropical outgassing in the ocean inversions used to
848 adjust our annual mean flux estimates (Fig. 8).

849 This dataset represents a significant advance over existing air-sea O_2 flux products by resolving
850 flux interannual variability, utilizing sophisticated ML-based DO fields that better capture
851 complex spatial and temporal patterns, and providing comprehensive uncertainty quantification
852 across multiple scales. Despite these advances, several opportunities remain for further

https://doi.org/10.5194/essd-2025-738
Preprint. Discussion started: 23 December 2025

improvement, including incorporation of high-latitude Arctic and coastal DO estimates that are currently absent from GOBAI-O_2 products, collection of DO data in underrepresented areas (e.g., Indian Ocean and high-latitudes), continued development of ML algorithms to better handle sparse and heterogeneous ocean observations, and refinement of bubble-mediated flux parameterizations. The resulting flux product offers substantial value across multiple research communities and applications. It can be used to improve atmospheric inversions on terrestrial and oceanic carbon cycles. It can serve as critical benchmarks for evaluating ocean biogeochemical models and atmospheric transport models. We provide this product for community use.

https://doi.org/10.5194/essd-2025-738
Preprint. Discussion started: 23 December 2025

Appendix A. Gas-exchange parameterization

The W97 method determines the net air-sea O_2 flux (F_T, mol m^{-2} s^{-1}) by combining the diffusive and bubble-mediated fluxes, following

$$F_T = (k_s + k_b) \cdot \left([O_2]_{adj} - (1 + \Delta_e)[O_2^{sat}]\right) \cdot \rho_w \times 10^{-6}, \quad (A1)$$

where $[O_2]_{adj}$ (µmol $kgsw^{-1}$) is the adjusted mixed-layer-averaged DO concentration (Section 2.4). $[O_2^{sat}]$ (µmol $kgsw^{-1}$) is the DO saturation concentration calculated following Garcia and Gordon (1992). k_s and k_b (m s^{-1}) are the gas exchange velocity due to diffusive and bubble processes, respectively. Δ_e is the bubble-induced supersaturation, according to Woolf and Thorpe (1991). ρ_w (kg m^{-3}) is the seawater density as a function of temperature and salinity. The factor of 10^{-6} is to convert the unit from µmol to mol. Here, we calculate

$$k_s = 1.57 \times 10^{-4} \cdot U_*^a \cdot \left(\frac{S_{O_2}}{660}\right)^{-0.5}, \quad (A2)$$

where U_*^a (m s^{-1}) is the friction velocity on the air side of the air-water interface, and is calculated based on the unitless drag coefficient (C_d) and 10-m wind speed (U_{10}) following

$$U_*^a = \sqrt{C_d} \cdot U_{10}, \quad (A3)$$

$$C_d = \begin{cases} 0.012 & (U_{10} < 11 \text{ m s}^{-1}) \\ (0.49 + 0.065 \cdot U_{10}) \times 10^{-3} & (11 \text{ m s}^{-1} \le U_{10} \le 20 \text{ m s}^{-1}) \\ 0.018 & (U_{10} > 20 \text{ m s}^{-1}) \end{cases}, \quad (A4)$$

and S_{O_2} is the unitless Schmidt number for O_2, calculated as a function of temperature, following Wanninkhof (2014).

k_b is calculated following

$$k_b = 14 \times 9.4 \times 10^{-3} \cdot U_{10}^{3.41} \cdot S_c^{-0.5}, \quad (A5)$$

in units of cm hr^{-1} and then converted to m s^{-1} by dividing by 360,000.

Δ_e is calculated following

https://doi.org/10.5194/essd-2025-738
Preprint. Discussion started: 23 December 2025

$$\Delta_e = 0.01 \left(\frac{U_{10}}{U^*_{10,O_2}} \right)^2, \tag{A6}$$

where U^*_{10,O_2} is the reference 10-m wind speed at which Δ_e is 1% for O_2, and is assumed to be 9.6 m s^{-1}, according to Woolf and Thorpe (1991).

For the L13 and S09 methods, the net flux calculation follows Eqs. 1-2. The diffusive flux (F_s) is calculated following

$$F_s = k_s \cdot \left([O_2]_{adj} - [O_2^{sat}] \right) \cdot \rho_w \times 10^{-6}, \tag{A7}$$

with

$$k_s = 1.3 \times 1.04 \times 10^{-4} \cdot U_*^a \cdot \left(\frac{S_{O_2}}{660} \right)^{-0.5} \tag{A8}$$

for the L13 method, and

$$k_s = 8.67 \times 10^{-7} \cdot U_{10}^2 \cdot \left(\frac{S_{O_2}}{660} \right)^{-0.5} \tag{A9}$$

for the S09 method.

In these two methods, F_c is calculated as the product of a mass transfer coefficient (k_c, mol m^{-2} s^{-1}) and O_2 atmospheric mole fraction ($X^{O_2} = 0.2094$), following

$$F_c = -k_c \cdot X^{O_2}, \tag{A10}$$

while F_p is calculated following

$$F_p = k_p \cdot ([O_2]_{adj} - (1 + \Delta_P) \cdot [O_2^{sat}]) \cdot \rho_w \times 10^{-6}, \tag{A11}$$

with k_p (m s^{-1}) as the gas exchange coefficient across the large bubble interface, and Δ_P as the bubble-produced increment of supersaturation.

For the L13 method, we have

https://doi.org/10.5194/essd-2025-738
Preprint. Discussion started: 23 December 2025

$$k_c = 5.56 \cdot (U_*^w)^{3.86}, \quad (A12)$$

$$k_p = 5.5 \cdot (U_*^w)^{2.76} \cdot \left(\frac{S_{O_2}}{660}\right)^{-\frac{2}{3}}, \quad (A13)$$

$$\Delta_P = 1.52 \cdot (U_*^w)^{1.06}. \quad (A14)$$

In Eqs. A12-14, U_*^w (m s^{-1}) represents the water-side friction velocity, and is calculated as

$$U_*^w = 0.034\sqrt{C_d} \cdot U_{10}. \quad (A15)$$

For the S09 method, we have

$$k_c = 9.1 \times 10^{-11} \frac{(P_a - P_{H_2O})X^{O_2}}{RT}(U_{10} - 2.27)^3 \quad (\text{mol m}^{-2}\text{s}^{-1}), \quad (A16)$$

$$k_p = 2.3 \times 10^{-3} \left(\frac{D^{O_2}}{D_0}\right)^{0.67} (U_{10} - 2.27)^3, \quad (A17)$$

$$\Delta P = \frac{\rho_w g z_b}{RT} \frac{\beta X^c}{[O_2^{sat}]}. \quad (A18)$$

P_a (Pa) is the atmospheric pressure at the sea surface and is assumed to be 101,325 Pa in our calculation. P_{H_2O} (Pa) is the equilibrium water vapor pressure, calculated as a function of temperature (Bolton, 1980), following

$$P_{H_2O} = 6.112 \cdot \exp\left(\frac{17.67 \cdot T_{air}}{T_{air} + 243.5}\right). \quad (A19)$$

D^{O_2} (m^2 s^{-1}) is the molecular diffusion coefficient for O_2, with values of 2×10^{-9} at 20°C and 1.25×10^{-9} at 0°C, and is assumed to vary linearly with temperature. T_{air} is the surface air temperature (°C) from ERA5 (Hersbach et al., 2020). D_0 (m^2 s^{-1}) is used to ensure unit balance and is equal to 1. R (m^3 Pa mol^{-1} K^{-1}) is the gas constant, assumed to be 8.314. T (K) is surface ocean temperature. With 10-m wind speed smaller than 2.27, k_c and k_p are set to 0. z_b (m) is the mean depth of large bubbles, calculated as a function of 10-m wind speed, following

$$z_b = (0.15U_{10} - 0.55), \quad (A20)$$

with negative z_b set to be 0.

https://doi.org/10.5194/essd-2025-738
Preprint. Discussion started: 23 December 2025

922 The Bunsen coefficient for O_2 (β) is determined from temperature (K) and salinity (PSU) using
923 the empirical relationship of Weiss (1970), following

924
$$\ln(\beta) = A_1 + A_2 \cdot \frac{100}{T} + A_3 \cdot \ln\left(\frac{T}{100}\right) + S \cdot \left[B_1 + B_2 \cdot \left(\frac{T}{100}\right) + B_3 \cdot \left(\frac{T}{100}\right)^2\right], \quad \text{(A21)}$$

925

926 where A_1 = -58.3877, A_2 = 85.8079, A_3 = 23.8439, B_1 = -0.034892, B_2 = 0.015568, and B_3 =
927 -0.0019387.

928 To illustrate flux differences from varying gas exchange parameterization schemes and wind
929 products, we show monthly climatologies with different parameterization schemes (Fig. A1,
930 using CCMP wind) and different wind products (Fig. A2, using the L13 scheme).

https://doi.org/10.5194/essd-2025-738
Preprint. Discussion started: 23 December 2025

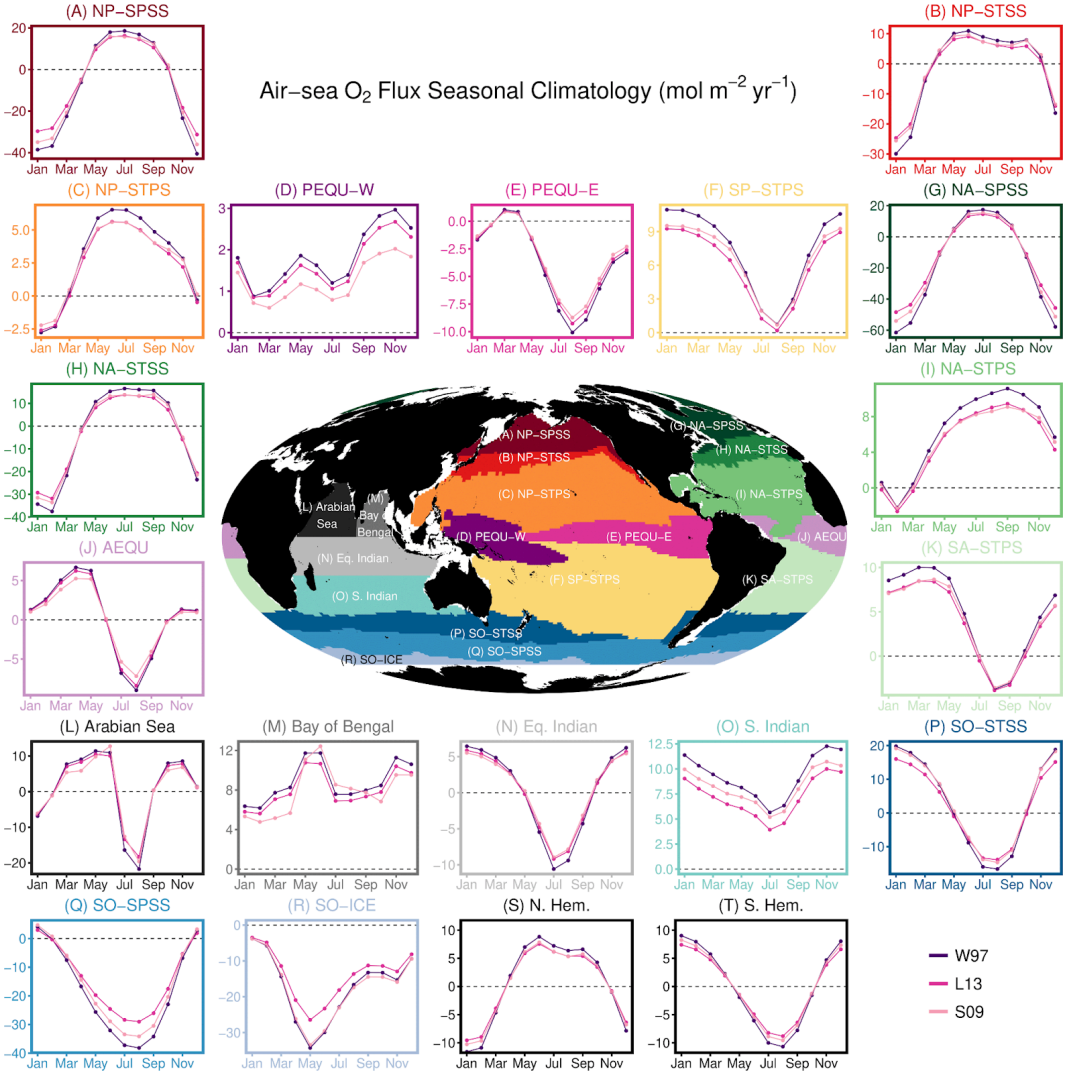

931 Fig. A1: Similar to Fig. 2, but showing comparisons of ensemble mean air-sea O_2 flux seasonal
932 climatologies for 20 RECCAP2 regions resolved using each of the three gas exchange
933 parameterization schemes (W97, L13, and S09) and the CCMP wind product.

https://doi.org/10.5194/essd-2025-738
Preprint. Discussion started: 23 December 2025

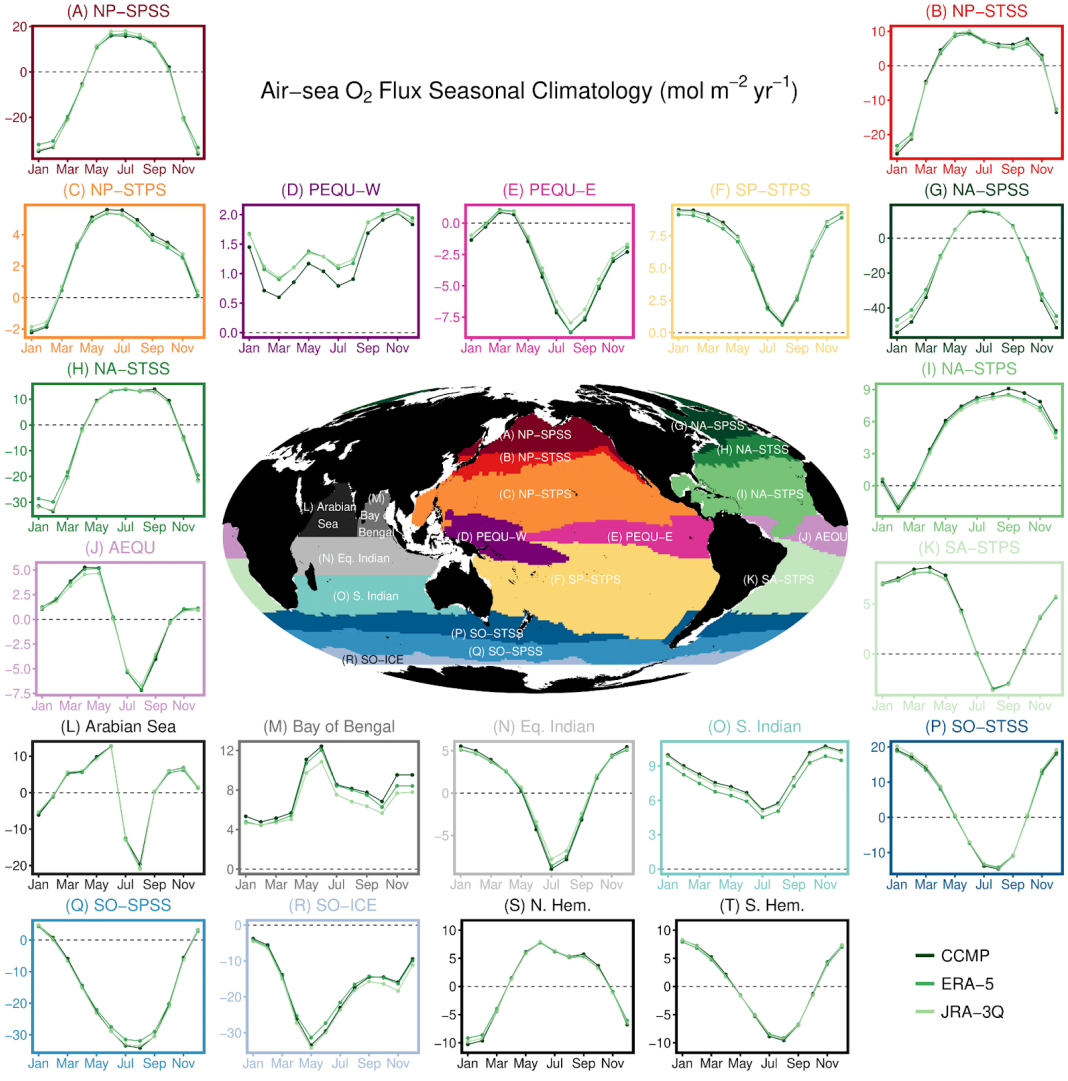

935

936 Fig. A2: Similar to Fig. 2, but showing comparisons of ensemble mean air-sea O_2 flux seasonal
937 climatologies for 20 RECCAP2 regions resolved using each of the three wind products (CCMP,
938 ERA-5, and JRA-3Q) and the L13 gas exchange parameterization scheme.

https://doi.org/10.5194/essd-2025-738
Preprint. Discussion started: 23 December 2025

Appendix B. Annual mean flux adjustment

We apply concentration adjustments to GOBAI-O_2 DO fields to force global and regional annual mean fluxes to match independent observation-based estimates. For the global annual flux (Z_{O_2}), we adopt the method in Keeling and Manning (2014), following

$$Z_{O_2} = \gamma_{O_2} \cdot Q + Z_{anthN}. \quad (B1)$$

In this equation, γ_{O_2} (4.8±2.6 nmol J^{-1}) is the O_2 flux to ocean heat flux ratio (Keeling and Garcia, 2002). Q is the net observed change in ocean heat content, computed by combining the 0 to 2 km depth range from the NCEI product (Levitus et al., 2012, 2017) and below-2km warming with a constant rate of change of 1.6 TW $year^{-1}$ (Desbruyères et al., 2016). Z_{anthN} is an additional term quantifying the outgassing due to nitrogen deposition, estimated to be 19±10 Tmol yr^{-1} (Keeling and Manning, 2014; Resplandy et al., 2019). This estimate effectively quantifies the expected annual O_2 flux due to solubility effects (i.e., ocean warming) and additional influences of ocean stratification and biology averaged over interannual to decadal time scales.

We calculate Z_{O_2} for each year after 1980. However, the raw annual values exhibit IAV with substantial uncertainties, driven primarily by fluctuations in ocean heat content. The relationship between ocean heat flux and O_2 flux in γ_{O_2} is more robust on decadal timescales than for IAV, as shorter-term variations in air-sea O_2 exchange can be influenced by ocean ventilation that are not directly coupled to heat uptake (Hamme and Keeling, 2008; Keeling and Garcia, 2002). To reduce this IAV and provide a constraint that better reflects the near-steady state heat-O_2 relationship, we calculate smoothed annual values by applying a weighted linear regression to the Z_{O_2} time series, with weights determined by the inverse square of the annual uncertainties. The uncertainty in the smoothed Z_{O_2} for each year incorporates the uncertainty in the fitted regression line itself, quantified by the standard error of the fitted values and the underlying uncertainties in the raw Z_{O_2} calculations. We combine these uncertainties in quadrature to obtain the total 1-σ uncertainty for each year. For 2024, where no raw Z_{O_2} calculation exists, we use the mean raw uncertainty from 2004-2023 as a representative estimate. The linear fit yields a Z_{O_2} in 2004 of 53±49.4 Tmol $year^{-1}$, and in 2024 of 70±33.1 Tmol $year^{-1}$, with a 2004-2024 average value of 61 Tmol $year^{-1}$. We report the raw Z_{O_2} and fitted value as well as uncertainties in Table B1.

https://doi.org/10.5194/essd-2025-738
Preprint. Discussion started: 23 December 2025

We also adjust regional annual mean fluxes to match ocean inversion model estimates of annual O_2 flux from Resplandy et al. (2016), which reported fluxes for 21 ocean basins from seven inversions. We only use five of the seven inversions (Table B2) that are selected based on their smaller tropical-southern ocean O_2 flux gradients with better agreement to atmospheric observations of O_2 gradients. Nevertheless, the five products still overestimate the tropical-extratropical flux gradient (Fig. 8). For each inversion, we integrate the flux into six large ocean regions (Fig. B1) rather than finer spatial scales to minimize abrupt changes in flux at regional boundaries (Table B2). These inversions represent only the pre-industrial steady state, which sum to near zero flux on the global scale. Because these inversions do not include regional variations in climate change impacts, our flux adjustments may not fully capture anthropogenic trends in air-sea O_2 fluxes that vary spatially.

For each ensemble iteration of flux estimation and for each year, we adjust the DO field by a set of constant values for each of the six ocean regions corresponding to a randomly selected inversion from the five available for individual regions (Table B2), and a global adjustment randomly sampled from Table B1. Adjusting the regional and global total fluxes every year removes the original flux IAV and trends from the raw flux product, while imposing smoothed global annual mean flux trends derived from the ocean heat flux constraint.

The adjustment for GOBAI-O_2 v2.3 (Fig. B2), averaged from 2004 to 2024, indicates that DO concentrations need to be adjusted downward across all six ocean regions, resulting in greater ocean O_2 uptake or reduced outgassing in the adjusted flux estimates. In descending order, the averaged adjustments are -3.50 μmol kg^{-1} for the North Atlantic, -3.25 μmol kg^{-1} for the North Pacific, -3.13 μmol kg^{-1} for the Indian Ocean, -2.54 μmol kg^{-1} for the Equatorial Atlantic, -2.12 μmol kg^{-1} for the Equatorial Pacific, and -0.30 μmol kg^{-1} for the Southern Ocean.

Over time, the adjustments show a trend toward larger reductions in DO concentrations in the Indian Ocean, while other regions exhibit no significant temporal trends. This pattern occurs because GOBAI-O_2 v2.3 DO concentrations in the Indian Ocean decrease faster than the corresponding decline in O_2 saturation calculated from temperature and salinity, which would produce an increasing trend in oceanic O_2 uptake without the annual mean flux adjustment.

https://doi.org/10.5194/essd-2025-738
Preprint. Discussion started: 23 December 2025

The adjustment pattern varies across the three GOBAI-O_2 versions (Figs. S10-11), which produce differences in mean DO over each ocean region. Despite these differences, all versions consistently indicate that the North Atlantic and North Pacific require the largest DO concentration reductions. The adjustments remain relatively small (< 2%) compared to annual average DO concentrations of approximately 350 µmol kg^{-1} in high-latitude regions and 200 µmol kg^{-1} in tropical oceans.

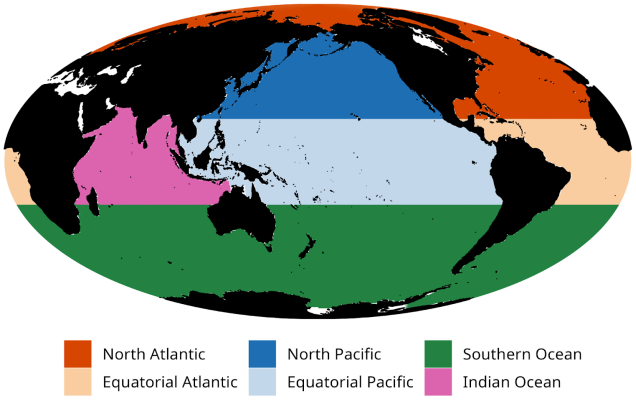

Fig. B1: Map of six ocean regions used to constrain annual mean fluxes through five ocean inversion estimates. Each colored region represents a distinct oceanic domain where region-specific inversion constraints are applied to adjust the calculated air-sea O_2 flux annual means. For each region, the target annual mean flux is integrated from finer-scale regions reported in Resplandy et al. (2016).

https://doi.org/10.5194/essd-2025-738
Preprint. Discussion started: 23 December 2025

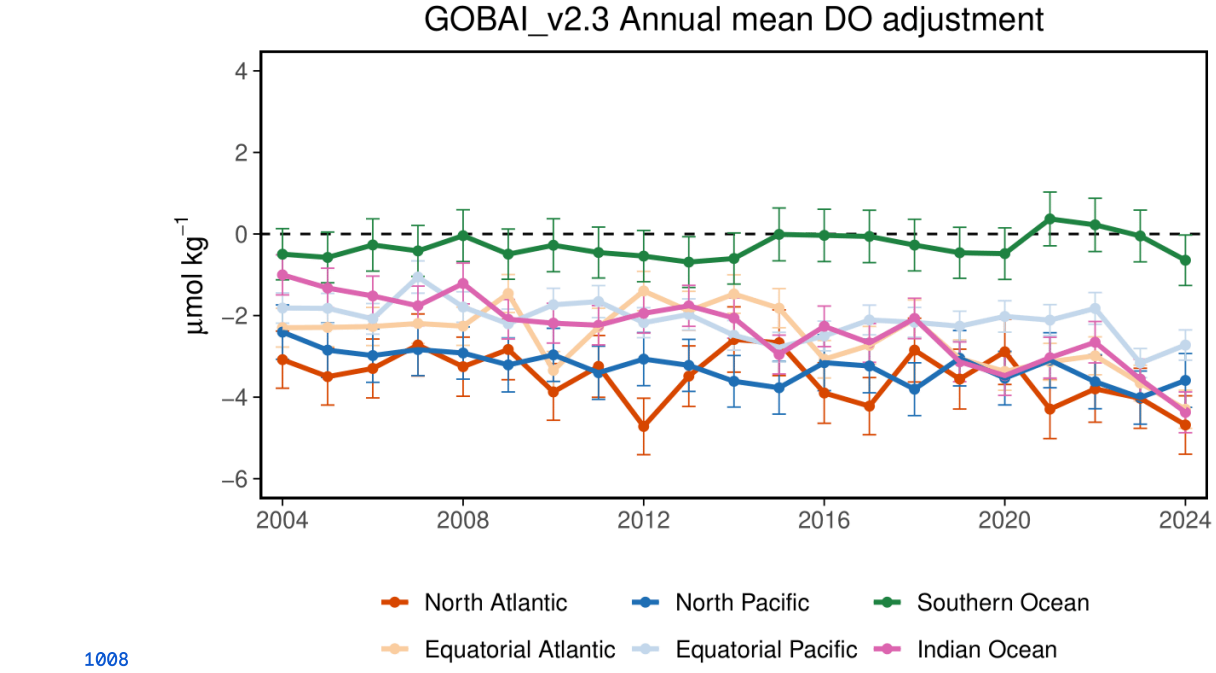

Fig. B2: Required annual mean DO adjustment for the six ocean regions (Fig. B1) by year, based on fluxes calculated using GOBAI-O_2 v2.3. These adjustments include both the global annual mean adjustment and the regional adjustments. Similar figures showing required annual mean DO adjustments for fluxes calculated using GOBAI-O_2 v2.1 and v2.2 are shown in Figs. S10–S11, which reveal significant differences compared to v2.3, highlighting the sensitivity of annual mean DO to ML methods.

https://doi.org/10.5194/essd-2025-738
Preprint. Discussion started: 23 December 2025

Open Access Earth System Science Data Discussions

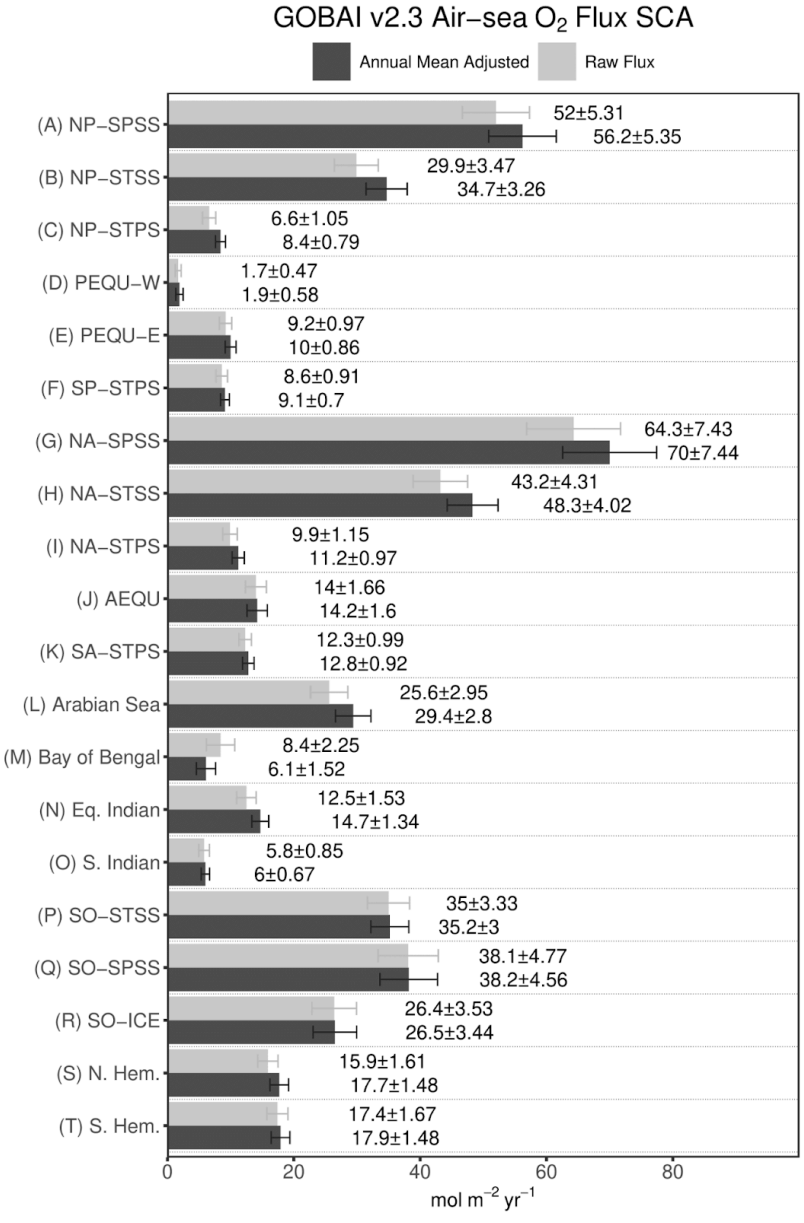

Fig. B3: Comparison of air-sea O_2 flux SCA for 20 RECCAP2 regions (see Fig. 3 caption for region definitions and map) calculated using raw fluxes (gray) versus fluxes from annual mean-adjusted DO (black). Values are shown in mol m^{-2} yr^{-1} based on GOBAI-O_2 v2.3. The ensemble 1-σ standard deviation is also shown. Annual mean flux adjustments affect the flux seasonal cycle because temporally constant DO adjustments interact with seasonally varying wind speeds in the gas exchange parameterization.

https://doi.org/10.5194/essd-2025-738
Preprint. Discussion started: 23 December 2025

Table B1: Global annual mean air-sea O_2 flux derived from ocean heat content changes with nitrogen deposition adjustment (Eq. B1). The original flux represents yearly estimates, while the smoothed flux is obtained from an uncertainty-weighted linear regression to smooth the original flux that has large IAV. We therefore use the smoothed flux to constrain our annual mean flux estimates. Uncertainties (1-σ) for the original flux incorporate errors in the O_2-to-heat flux ratio, global ocean heat content changes, and the nitrogen deposition adjustment. Uncertainties for the smoothed flux are calculated as the root sum of squares of the original flux uncertainty and the regression fit uncertainty.

Year	Original flux (Tmol year^{-1})		Smoothed flux (Tmol year^{-1})	
	Mean	1-σ	Mean	1-σ
2004	102	49.1	53	49.4
2005	35	25.3	54	25.7
2006	44	24.5	55	24.9
2007	38	23.3	56	23.7
2008	93	41.2	56	41.4
2009	48	25.4	57	25.7
2010	56	27.3	58	27.6
2011	94	42.0	59	42.1
2012	68	31.1	60	31.3
2013	94	41.0	61	41.2
2014	73	30.6	61	30.9
2015	76	32.9	62	33.2
2016	63	27.3	63	27.7
2017	38	19.5	64	20.1
2018	80	34.3	65	34.7
2019	80	34.2	66	34.6
2020	60	25.9	66	26.5
2021	112	48.0	67	48.4
2022	69	30.3	68	31.0
2023	64	31.5	69	32.3
2024			70	33.1

https://doi.org/10.5194/essd-2025-738
Preprint. Discussion started: 23 December 2025

Table B2. Area-integrated annual mean air-sea O_2 flux (Tmol) of six large regions (Fig. B1) estimated by five ocean inversions from Resplandy et al. (2016). Positive as ocean O_2 outgassing.

Regions	MOM-LHS	MOM-LL	MOM-PSS	MOM-RDS	MITgcm-ECCO
North Atlantic	-53.92	-64.95	-43.44	-50.99	-68.56
Equatorial Atlantic	37.07	38.27	42.74	45.91	36.70
North Pacific	-25.27	-25.95	-42.96	-33.18	-32.62
Equatorial Pacific	78.31	78.70	91.59	107.69	106.17
Southern Ocean	-66.01	-55.79	-61.24	-106.79	-74.98
Indian Ocean	31.66	32.07	15.30	39.38	34.17
Global Sum	1.84	2.35	1.99	2.02	0.88

https://doi.org/10.5194/essd-2025-738
Preprint. Discussion started: 23 December 2025

Appendix C. Atmospheric APO measurements, non-oceanic O_2 flux corrections, and uncertainty

The surface station APO observations are from the Scripps O_2 program (Keeling, 2019). We use roughly bi-weekly flask $\delta(O_2/N_2)$ and CO_2 data (Eq. 5) collected during clean background air conditions from 10 sampling sites along the Pacific (map shown in Fig. S1A). Flask samples are analyzed at Scripps using a custom interferometer and a non-dispersive infrared analyzer . The sample times match the NOAA ObsPack CO_2 files from the Scripps O_2 Program (Schuldt et al., 2021).

APO observations in per meg units can be broken down into contributions from air-sea O_2 (O_2^{ocn}), air-sea CO_2 (CO_2^{ocn}), air-sea N_2 (N_2^{ocn}), fossil fuel O_2 (O_2^{ff}), and fossil fuel CO_2 (CO_2^{ff}) fluxes, following

$$\mathrm{APO} = \frac{1}{X_{O_2}}\Delta O_2^{ocn} + \frac{1.1}{X_{O_2}}\Delta CO_2^{ocn} - \frac{1}{X_{N_2}}\Delta N_2^{ocn} + \frac{1}{X_{O_2}}\Delta O_2^{ff} + \frac{1.1}{X_{O_2}}\Delta CO_2^{ff}, \qquad (C1)$$

where X_{O_2} (0.2094) and X_{N_2} (0.7808) are the mole fractions of O_2 and N_2 in the atmosphere, and Δ represents deviation in the atmospheric concentration of a tracer in units of ppm created by the corresponding fluxes. Dividing by X_{O_2} or X_{N_2} converts the unit from ppm-equivalent to per meg. For each tracer component on the RHS of Eq. C1, except O_2^{ocn}, which is our target, we use model forward transport of flux fields sampled at measurement locations and times. For each tracer, we employ two different flux products and four different transport models from the APO forward transport model intercomparison project (APO-MIP1, Jin et al., 2025). The sum of the last two terms in Eq. C1 forms ΔAPO^{ff}, which represents APO changes due to fossil fuel burning.

For CO_2^{ocn}, we use a configuration of the Community Earth System Model (CESM2) Forced Ocean-Sea-Ice (FOSI) simulation (Yeager et al., 2022) and a ML interpolation of pCO_2 based air-sea CO_2 fluxes (Jersild et al., 2017; Landschützer et al., 2016).

For N_2^{ocn}, we use two flux products ($F^{N_2^{ocn}}$) derived by scaling ocean heat flux from ERA5 reanalyses (Hersbach et al., 2020) and CESM2, following

https://doi.org/10.5194/essd-2025-738
Preprint. Discussion started: 23 December 2025

$$F^{N_2^{ocn}} = \frac{1}{1.3}\frac{dS}{dT}\frac{Q}{C_p}, \quad (C2)$$

where dS/dT (mol kg^{-1} C^{-1}) is the temperature derivative of solubility using solubility coefficients from Hamme & Emerson (2004). C_p represents the specific heat capacity of seawater, which is assumed to be 3993 J kg^{-1} C^{-1}. The factor of 1/1.3 is to adjust the seasonal amplitude as proposed by Jin et al. (2007).

For O_2^{ff} and CO_2^{ff}, we use fossil CO_2 emission and O_2 uptake fluxes from Jones et al. (2021), and CO_2 emission as prepared for the OCO-2 Model Intercomparison Project (MIP) version 10, downloaded from Basu & Nassar (2021). For the second product, O_2 combustion is not available, but we estimate O_2^{ff} by scaling the atmospheric field of CO_2^{ff} by a factor of -1.4 (Keeling, 1988; Steinbach et al., 2011).

We use four transport models. These include two versions of NICAM-TM, based on the Nonhydrostatic Icosahedral Atmospheric Model (NICAM) (Niwa et al., 2011; Satoh et al., 2014); MIROC4-ACTM, a new generation Model for Interdisciplinary Research on Climate (MIROC, version 4.0; Watanabe et al., 2008); the atmospheric general circulation model (AGCM)-based chemistry-transport model (ACTM; Patra et al., 2018); and CAMS_LMDZ, an offline transport model from the Atmospheric General Circulation Model of Laboratoire de Météorologie Dynamique, called LMDz. Detailed descriptions of these models are available in Jin et al. (2025).

We use airborne APO data from the NSF NCAR GV aircraft during the HIAPER Pole-to-Pole Observations (HIPPO, Wofsy, 2011) project from 2009-2011, the O_2/N_2 Ratio and CO_2 Airborne Southern Ocean Study (ORCAS, Stephens et al., 2018) in January and February of 2016, and the NASA DC-8 aircraft during the Atmospheric Tomography Mission (ATom, Thompson et al., 2022) from 2016 to 2018. HIPPO consisted of five campaigns along a Pacific transect, ATom consisted of four campaigns covering both Pacific and Atlantic transects, and the six-week ORCAS campaign provided dense sampling over the Drake Passage and ocean areas adjacent to the tip of South America and the Antarctic Peninsula. The horizontal flight tracks are shown in Fig. S1B-D.

https://doi.org/10.5194/essd-2025-738
Preprint. Discussion started: 23 December 2025

Airborne APO measurements were made with the NSF NCAR Airborne Oxygen Instrument (AO2), using a vacuum-ultraviolet absorption technique to measure O_2 and a single-cell infrared gas analyzer to measure CO_2 (Stephens et al., 2021g). AO2 produces measurements every 2.5 s, which are averaged to 10 sec frequency for merging with other aircraft data. Airborne data are also selected to match with the ObsPack CO_2 files. The AO2 measurements were adjusted on a per flight basis to agree with air samples collected during flight by the NSF NCAR/Scripps Medusa flask sampler, which captures 32 samples per flight for subsequent laboratory analysis at Scripps (Bent, 2014; Stephens et al., 2021g). These flask samples help identify and correct time-dependent systematic biases in the continuous measurements. Before being used as a reference, the Medusa data underwent their own adjustment process to minimize diffusive fractionation effects inherent in flask sampling by applying an Ar/N_2 correction following

$$\delta\left(\frac{O_2}{N_2}\right)^{*} = \delta\left(\frac{O_2}{N_2}\right)_{obs} - \frac{1}{3.77}[\delta\left(\frac{Ar}{N_2}\right)_{obs} - 15], \quad \text{(C3)}$$

where $\delta(O_2/N_2)_{obs}$ and $\delta(Ar/N_2)_{obs}$ represent Medusa flask measurements (Stephens et al., 2021g). The coefficient 3.77 represents the theoretical ratio between $\delta(Ar/N_2)$ and $\delta(O_2/N_2)$ variations resulting from thermal fractionation processes (Keeling et al., 2004; Stephens et al., 2021g), and is applied consistently across all campaigns. The constant 15 per meg is the approximate global surface mean value from the Scripps stations on the Scripps Ar/N_2 scale. The corrected $\delta(O_2/N_2)^{*}$ has reduced sensitivity to both thermal and pressure-gradient fractionation artifacts arising from airborne sampling and laboratory analysis.

Therefore, our AO2 APO measurements adjusted to match Medusa data are effectively APO^{*} that contains $\delta(Ar/N_2)$, following

$$APO^{*} = APO - \frac{1}{3.77}\delta\left(\frac{Ar}{N_2}\right)_{obs.} \quad \text{(C4)}$$

The $\delta(Ar/N_2)$ adjustment has minimal impact on the APO annual mean value, but it scales down the APO seasonal cycle amplitude by about 4% (Jin et al., 2025). We correct for this $\delta(Ar/N_2)$ component of APO^{*} by including an extra Ar/N_2 correction, which is scaled from the N_2^{ocn} correction (Jin et al., 2023), following

https://doi.org/10.5194/essd-2025-738
Preprint. Discussion started: 23 December 2025

$$\delta\left(\frac{\mathrm{Ar}}{\mathrm{N_2}}\right) = \frac{1}{\mathrm{X_{Ar}}}\Delta\mathrm{Ar} - \frac{1}{\mathrm{X_{N_2}}}\Delta\mathrm{N_2}$$
$$= \frac{1}{\mathrm{X_{Ar}} \cdot 34}\Delta\mathrm{N_2} - \frac{1}{\mathrm{X_{N_2}}}\Delta\mathrm{N_2} \qquad \text{(C5)}$$
$$= 1.87 \cdot \Delta\mathrm{N_2^{ocn}} \quad ,$$

where X_{Ar} (0.00934) is the mole fraction of Ar in the atmosphere. 1/34 is a scaling factor, which is the ratio of Ar and N_2 air-sea fluxes driven by heat flux from Table 3 in (Manizza et al., 2012).

Therefore, to correct for the non-oceanic O_2 flux contribution in airborne APO* data, we adapt Eq. C1 following

$$\mathrm{APO^*} = \frac{1}{\mathrm{X_{O_2}}}\Delta\mathrm{O_2^{ocn}} + \frac{1.1}{\mathrm{X_{O_2}}}\Delta\mathrm{CO_2^{ocn}} - \frac{1}{\mathrm{X_{N_2}}}\Delta\mathrm{N_2^{ocn}} - \frac{1.87}{3.77}\Delta\mathrm{N_2^{ocn}} + \frac{1}{\mathrm{X_{O_2}}}\Delta\mathrm{O_2^{ff}} + \frac{1.1}{\mathrm{X_{O_2}}}\Delta\mathrm{CO_2^{ff}} \quad . \qquad \text{(C6)}$$

using the same fluxes and forward atmospheric transport as described above. To quantify the uncertainty of $\mathrm{O_2^{ocn}}$, we generate a large ensemble of station and airborne $\Delta\mathrm{O_2^{ocn}}$. We first generate a large ensemble (1000 members) of observation data. For airborne APO* data, we consider uncertainty due to measurement imprecision and reproducibility (Stephens et al., 2021g), and the uncertainty of the land biosphere O_2:CO_2 exchange ratio. For station APO data, we generate a large ensemble of measurements using an error model that considers a span error of 1% in the laboratory calibration scale (Keeling et al., 2020) and long-term reference cylinder effects including corrosion error of ±0.3 per meg yr^{-1}, leakage error of ±0.2 per meg yr^{-1}, and desorption error of ±0.1 per meg yr^{-1} (Keeling et al., 2007). These systematic errors are held constant across all stations for each ensemble member. In addition, for each individual flask measurement, we add a random analytical error of ±3.3 per meg and a thermal fractionation error of ±2 per meg. Using two air-sea CO_2 flux products, two air-sea N_2 flux products, two fossil fuel O_2 and CO_2 flux products, and four atmospheric transport models, we generate 32 unique non-oceanic O_2 flux correction combinations. We apply each combination to the station APO or airborne APO* large ensemble, leading to 32,000 estimates of $\Delta\mathrm{O_2^{ocn}}$. The uncertainty of the $\Delta\mathrm{O_2^{ocn}}$ seasonal cycle and annual mean value at each station and for the latitudinally-binned airborne tropospheric-average is then calculated as the 1-σ ensemble spread. We note that these non-oceanic O_2 flux corrections have a small impact on the APO seasonal cycle (Fig. C1), but that the annual mean component of APO is particularly sensitive to the air-sea CO_2 flux and

https://doi.org/10.5194/essd-2025-738
Preprint. Discussion started: 23 December 2025

fossil fuel O_2 and CO_2 fluxes (Fig. 7). For this reason, and because our atmospheric transport model simulations have arbitrary background concentrations, we can not compare the global annual-mean observed ΔO_2^{ocn} to forward transport simulations of our flux product. Thus, the meridional tropospheric-average gradient comparison shown in Fig. 8 includes an arbitrary global-mean adjustment that sets global mean concentrations to zero.

https://doi.org/10.5194/essd-2025-738
Preprint. Discussion started: 23 December 2025

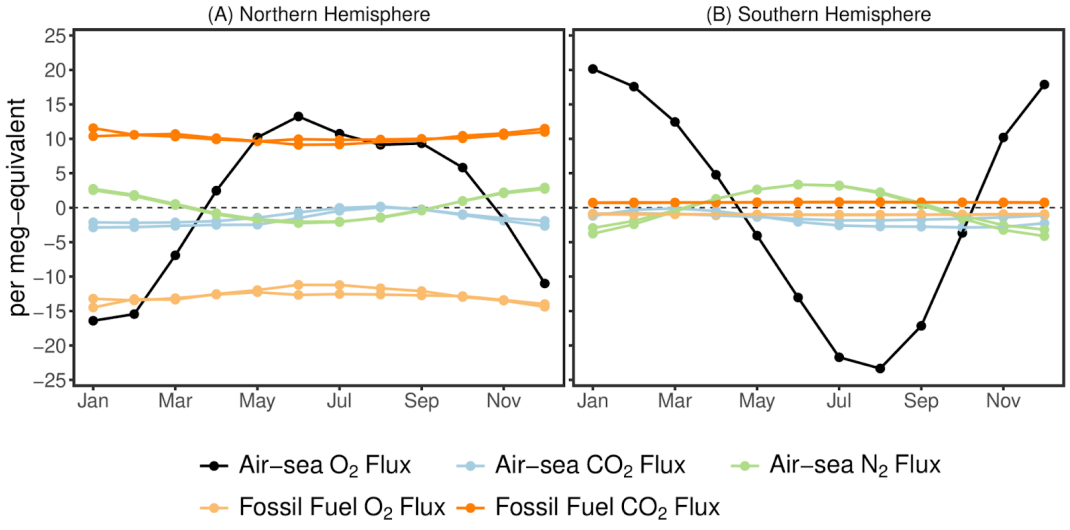

Fig. C1: Monthly climatology (2004–2024) of hemispheric ensemble mean air-sea O_2 flux (black) compared to non-oceanic flux correction components (2004–2020 average) used to correct APO observations. Each flux component (Tmol day^{-1}) creates an atmospheric tracer concentration in ppm units, which can be further converted to per meg units through scaling (Eq. C1). Here, we scale each flux component (Eq. C1) to directly show its contribution to observed APO in the per meg-equivalent unit. Note that air-sea N_2 flux is sign-reversed according to Eq. C1. The comparison demonstrates that the non-oceanic O_2 flux components have much smaller seasonal variations compared to the dominant air-sea O_2 flux that drives the observed APO seasonal cycle.

https://doi.org/10.5194/essd-2025-738
Preprint. Discussion started: 23 December 2025

Data Availability

All datasets used in this study are listed in Table 3 with their DOIs.

Table 3: Datasets DOIs.

Datasets	DOI	Reference
GOBAI-O_2-Flux (adjusted and raw	https://zenodo.org/records/17765275	(Jin, 2025)
GOBAI-O_2 (all versions)	https://doi.org/10.25921/z72m-yz67	(Sharp et al., 2022)
Scripps O_2 network surface observations	https://doi.org/10.6075/J0WS8RJR	(Keeling, 2019)
HIPPO 10-second merge data	https://doi.org/10.3334/CDIAC/HIPPO_010	(Wofsy, 2017)
Updated HIPPO1 AO2 measurements	https://doi.org/10.5065/D6J38QVV	(Stephens et al., 2021a)
Updated HIPPO2 AO2 measurements	https://doi.org/10.5065/D65Q4TF0	(Stephens et al., 2021b)
Updated HIPPO3 AO2 measurements	https://doi.org/10.5065/D67H1GXJ	(Stephens et al., 2021c)
Updated HIPPO4 AO2 measurements	https://doi.org/10.5065/D679431D	(Stephens et al., 2021d)
Updated HIPPO5 AO2 measurements	https://doi.org/10.5065/D6WW7G0D	(Stephens et al., 2021e)
ORCAS 10-second merge data	https://doi.org/10.5065/D6SB445X	(Stephens, 2017)
Updated ORCAS AO2 measurements	https://doi.org/10.5065/D6N29VC6	(Stephens et al., 2021f)
ATom 10-second merge data	https://doi.org/10.3334/ORNLDAAC/1925	(Wofsy, 2021)
APO-MIP1 simulation	https://doi.org/10.5065/f3pw-a676	(Stephens et al., 2025)

https://doi.org/10.5194/essd-2025-738
Preprint. Discussion started: 23 December 2025

Acknowledgements

Atmospheric O_2 measurements on HIPPO were supported by NSF grants ATM-0628519 and ATM-0628388. ORCAS was supported by NSF grants PLR-1501993, PLR-1502301, PLR-1501997, and PLR-1501292. Atmospheric O_2 measurements on ATom 1 were supported by NSF grants AGS-1547626 and AGS-1547797. Atmospheric O_2 measurements on ATom 2-4 were supported by NSF grants AGS-1623745 and AGS-1623748. The recent atmospheric measurements of the Scripps O_2 program have been supported via funding from the NSF and the National Oceanographic and Atmospheric Administration (NOAA) under Grants OPP-1922922, OPP-2329254, and NA20OAR4320278, respectively. We acknowledge atmospheric transport modelers, including Jesse Vance and Matthew Long (CAM-SD), Yosuke Niwa (NICAM), and Prabir K. Patra (MIROC4-ACTM), for providing atmospheric simulations of APO components. YJ would like to acknowledge the Advanced Study Program Postdoctoral Fellowship of the NSF National Center for Atmospheric Research. This material is based upon work supported by the NSF National Center for Atmospheric Research, which is a major facility sponsored by the U.S. National Science Foundation under Cooperative Agreement No. 1852977. M.M. acknowledges support from NASA (IDS-#19-0113) and NSF (OPP-192292 and OCE-2049294) and he was also supported by the National Recovery and Resilience Plan project TeRABIT (Terabit network for Research and Academic Big data in Italy - IR0000022 - PNRR Missione 4, Componente 2, Investimento 3.1 CUP I53C21000370006) in the frame of the European Union - NextGenerationEU funding. The development of GOBAI-O_2 and the work of J.D.S. has been supported by the Cooperative Institute for Climate, Ocean, & Ecosystem Studies at the University of Washington under NOAA cooperative agreement NA20OAR4320271 (CICOES contribution no. 2025-1503), by NOAA's Pacific Marine Environmental Laboratory (PMEL contribution no. 5959), and by NOAA's National Marine Fisheries Service under the Essential Data Acquisition efforts of the Inflation Reduction Act via award NA24NMFX405C0016-T1-01.

Author Contributions

Y.J. conceived of the project, conducted the analysis, generated the data products and figures, and wrote the paper. E.M. and B.S. provided atmospheric O_2 measurements. J.S. provided the GOBAI-O_2 product. All authors contributed to reviewing and editing the text.

https://doi.org/10.5194/essd-2025-738
Preprint. Discussion started: 23 December 2025

Competing Interests

The contact author has declared that none of the authors have any competing interests.

References

Atamanchuk, D., Koelling, J., Send, U., and Wallace, D. W. R.: Rapid transfer of oxygen to the deep ocean mediated by bubbles, Nat. Geosci., 13, 232–237, https://doi.org/10.1038/s41561-020-0532-2, 2020.

Banerjee, P. and Kumar, P. S.: Dust-induced episodic phytoplankton blooms in the Arabian Sea during winter monsoon, J. Geophys. Res. Oceans, 119, 7123–7138, https://doi.org/10.1002/2014JC010304, 2014.

Basu, S. and Nassar, R.: Fossil Fuel CO_2 Emissions for the OCO2 Model Intercomparison Project (MIP) (2020.1), https://doi.org/10.5281/zenodo.4776925, 2021.

Bates, D., Mächler, M., Bolker, B., and Walker, S.: Fitting Linear Mixed-Effects Models Using **lme4**, J. Stat. Softw., 67, https://doi.org/10.18637/jss.v067.i01, 2015.

Battle, M., Fletcher, S. M., Bender, M. L., Keeling, R. F., Manning, A. C., Gruber, N., Tans, P. P., Hendricks, M. B., Ho, D. T., Simonds, C., Mika, R., and Paplawsky, B.: Atmospheric potential oxygen: New observations and their implications for some atmospheric and oceanic models, Glob. Biogeochem. Cycles, 20, GB1010, https://doi.org/10.1029/2005GB002534, 2006.

Behrenfeld, M. J., Boss, E., Siegel, D. A., and Shea, D. M.: Carbon-based ocean productivity and phytoplankton physiology from space, Glob. Biogeochem. Cycles, 19, GB1006, https://doi.org/10.1029/2004GB002299, 2005.

Bender, M. L., Ho, D. T., Hendricks, M. B., Mika, R., Battle, M. O., Tans, P. P., Conway, T. J., Sturtevant, B., and Cassar, N.: Atmospheric O_2/N_2 changes, 1993–2002: Implications for the partitioning of fossil fuel CO_2 sequestration, Glob. Biogeochem. Cycles, 19, GB4017, https://doi.org/10.1029/2004GB002410, 2005.

Bent, J.: Airborne Oxygen Measurements over the Southern Ocean as an Integrated Constraint of Seasonal Biogeochemical Processes, University of California, San Diego, 2014.

Bittig, H., Carval, T., and the Coriolis Argo data management team: BGC-Argo synthetic profile file processing and format on Coriolis GDAC (v1.3), https://doi.org/10.13155/55637, 2022.

Bolton, D.: The Computation of Equivalent Potential Temperature, Mon. Weather Rev., 108, 1046–1053, https://doi.org/10.1175/1520-0493(1980)108%3C1046:TCOEPT%3E2.0.CO;2, 1980.

Boyer, T., Conkright, M. E., and Levitus, S.: Seasonal variability of dissolved oxygen, percent

https://doi.org/10.5194/essd-2025-738
Preprint. Discussion started: 23 December 2025

oxygen saturation, and apparent oxygen utilization in the Atlantic and Pacific Oceans, Deep Sea Res. Part Oceanogr. Res. Pap., 46, 1593–1663, https://doi.org/10.1016/S0967-0637(99)00021-7, 1999.

Brandt, P., Alory, G., Awo, F. M., Dengler, M., Djakouré, S., Imbol Koungue, R. A., Jouanno, J., Körner, M., Roch, M., and Rouault, M.: Physical processes and biological productivity in the upwelling regions of the tropical Atlantic, Ocean Sci., 19, 581–601, https://doi.org/10.5194/os-19-581-2023, 2023.

Breitburg, D., Levin, L. A., Oschlies, A., Grégoire, M., Chavez, F. P., Conley, D. J., Garçon, V., Gilbert, D., Gutiérrez, D., Isensee, K., Jacinto, G. S., Limburg, K. E., Montes, I., Naqvi, S. W. A., Pitcher, G. C., Rabalais, N. N., Roman, M. R., Rose, K. A., Seibel, B. A., Telszewski, M., Yasuhara, M., and Zhang, J.: Declining oxygen in the global ocean and coastal waters, Science, 359, https://doi.org/10.1126/science.aam7240, 2018.

Busecke, J. J. M., Resplandy, L., Ditkovsky, S. J., and John, J. G.: Diverging Fates of the Pacific Ocean Oxygen Minimum Zone and Its Core in a Warming World, AGU Adv., 3, e2021AV000470, https://doi.org/10.1029/2021AV000470, 2022.

Bushinsky, S. M. and Emerson, S. R.: Biological and physical controls on the oxygen cycle in the Kuroshio Extension from an array of profiling floats, Deep Sea Res. Part Oceanogr. Res. Pap., 141, 51–70, https://doi.org/10.1016/j.dsr.2018.09.005, 2018.

Bushinsky, S. M., Gray, A. R., Johnson, K. S., and Sarmiento, J. L.: Oxygen in the Southern Ocean From Argo Floats: Determination of Processes Driving Air-Sea Fluxes, J. Geophys. Res. Oceans, 122, 8661–8682, https://doi.org/10.1002/2017JC012923, 2017.

Bushinsky, S. M., Nachod, Z., Fassbender, A. J., Tamsitt, V., Takeshita, Y., and Williams, N.: Offset Between Profiling Float and Shipboard Oxygen Observations at Depth Imparts Bias on Float pH and Derived pCO_2, Glob. Biogeochem. Cycles, 39, e2024GB008185, https://doi.org/10.1029/2024GB008185, 2025.

Cheng, L., Trenberth, K. E., Fasullo, J., Boyer, T., Abraham, J., and Zhu, J.: Improved estimates of ocean heat content from 1960 to 2015, Sci. Adv., 3, https://doi.org/10.1126/sciadv.1601545, 2017.

De Boyer Montégut, C., Madec, G., Fischer, A. S., Lazar, A., and Iudicone, D.: Mixed layer depth over the global ocean: An examination of profile data and a profile-based climatology, J. Geophys. Res. Oceans, 109, C12003, https://doi.org/10.1029/2004JC002378, 2004.

Deike, L., Zhou, X., Rustogi, P., Stanley, R. H. R., Reichl, B. G., Bushinsky, S. M., and Resplandy, L.: A universal wind–wave–bubble formulation for air–sea gas exchange and its impact on oxygen fluxes, Proc. Natl. Acad. Sci., 122, e2419319122, https://doi.org/10.1073/pnas.2419319122, 2025.

Desbruyères, D. G., Purkey, S. G., McDonagh, E. L., Johnson, G. C., and King, B. A.: Deep and abyssal ocean warming from 35 years of repeat hydrography, Geophys. Res. Lett., 43, 10,356-10,365, https://doi.org/10.1002/2016GL070413, 2016.

https://doi.org/10.5194/essd-2025-738
Preprint. Discussion started: 23 December 2025

Eddebbar, Y. A., Long, M. C., Resplandy, L., Rödenbeck, C., Rodgers, K. B., Manizza, M., and Keeling, R. F.: Impacts of ENSO on air-sea oxygen exchange: Observations and mechanisms, Glob. Biogeochem. Cycles, 31, 901–921, https://doi.org/10.1002/2017GB005630, 2017.

Emerson, S.: Seasonal oxygen cycles and biological new production in surface waters of the subarctic Pacific Ocean, J. Geophys. Res. Oceans, 92, 6535–6544, https://doi.org/10.1029/JC092iC06p06535, 1987.

Emerson, S. and Bushinsky, S.: The role of bubbles during air-sea gas exchange, J. Geophys. Res. Oceans, 121, 4360–4376, https://doi.org/10.1002/2016JC011744, 2016.

Fine, R. A., Lukas, R., Bingham, F. M., Warner, M. J., and Gammon, R. H.: The western equatorial Pacific: A water mass crossroads, J. Geophys. Res. Oceans, 99, 25063–25080, https://doi.org/10.1029/94JC02277, 1994.

Friedlingstein, P., O'Sullivan, M., Jones, M. W., Andrew, R. M., Hauck, J., Landschützer, P., Le Quéré, C., Li, H., Luijkx, I. T., Olsen, A., Peters, G. P., Peters, W., Pongratz, J., Schwingshackl, C., Sitch, S., Canadell, J. G., Ciais, P., Jackson, R. B., Alin, S. R., Arneth, A., Arora, V., Bates, N. R., Becker, M., Bellouin, N., Berghoff, C. F., Bittig, H. C., Bopp, L., Cadule, P., Campbell, K., Chamberlain, M. A., Chandra, N., Chevallier, F., Chini, L. P., Colligan, T., Decayeux, J., Djeutchouang, L. M., Dou, X., Duran Rojas, C., Enyo, K., Evans, W., Fay, A. R., Feely, R. A., Ford, D. J., Foster, A., Gasser, T., Gehlen, M., Gkritzalis, T., Grassi, G., Gregor, L., Gruber, N., Gürses, Ö., Harris, I., Hefner, M., Heinke, J., Hurtt, G. C., Iida, Y., Ilyina, T., Jacobson, A. R., Jain, A. K., Jarníková, T., Jersild, A., Jiang, F., Jin, Z., Kato, E., Keeling, R. F., Klein Goldewijk, K., Knauer, J., Korsbakken, J. I., Lan, X., Lauvset, S. K., Lefèvre, N., Liu, Z., Liu, J., Ma, L., Maksyutov, S., Marland, G., Mayot, N., McGuire, P. C., Metzl, N., Monacci, N. M., Morgan, E. J., Nakaoka, S.-I., Neill, C., Niwa, Y., Nützel, T., Olivier, L., Ono, T., Palmer, P. I., Pierrot, D., Qin, Z., Resplandy, L., Roobaert, A., Rosan, T. M., Rödenbeck, C., Schwinger, J., Smallman, T. L., Smith, S. M., Sospedra-Alfonso, R., Steinhoff, T., et al.: Global Carbon Budget 2024, Earth Syst. Sci. Data, 17, 965–1039, https://doi.org/10.5194/essd-17-965-2025, 2025.

Garcia, H. E. and Gordon, L. I.: Oxygen solubility in seawater: Better fitting equations, Limnol. Oceanogr., 37, 1307–1312, https://doi.org/10.4319/lo.1992.37.6.1307, 1992.

Garcia, H. E. and Keeling, R. F.: On the global oxygen anomaly and air-sea flux, J. Geophys. Res. Oceans, 106, 31155–31166, https://doi.org/10.1029/1999JC000200, 2001.

Garcia, H. E., Wang, Z., Bouchard, C., Cross, S. L., Paver, C. R., Reagan, J. R., Boyer, T. P., Locarnini, R. A., Mishonov, A. V., Baranova, O. K., Seidov, D., and Dukhovskoy, D.: World Ocean Atlas 2023, Volume 3: Dissolved Oxygen, Apparent Oxygen Utilization, Dissolved Oxygen Saturation and 30-year Climate Normal, https://doi.org/10.25923/rb67-ns53, 2024.

Gouretski, V., Cheng, L., Du, J., Xing, X., Chai, F., and Tan, Z.: A consistent ocean oxygen profile dataset with new quality control and bias assessment, Earth Syst. Sci. Data, 16, 5503–5530, https://doi.org/10.5194/essd-16-5503-2024, 2024.

Gruber, N., Gloor, M., Fan, S., and Sarmiento, J. L.: Air-sea flux of oxygen estimated from bulk data: Implications For the marine and atmospheric oxygen cycles, Glob. Biogeochem. Cycles,

https://doi.org/10.5194/essd-2025-738
Preprint. Discussion started: 23 December 2025

15, 783–803, https://doi.org/10.1029/2000GB001302, 2001.

Hamme, R. C. and Emerson, S. R.: The solubility of neon, nitrogen and argon in distilled water and seawater, Deep Sea Res. Part Oceanogr. Res. Pap., 51, 1517–1528, https://doi.org/10.1016/j.dsr.2004.06.009, 2004.

Hamme, R. C. and Keeling, R. F.: Ocean ventilation as a driver of interannual variability in atmospheric potential oxygen, Tellus B Chem. Phys. Meteorol., 60, 706–717, https://doi.org/10.1111/j.1600-0889.2008.00376.x, 2008.

Hayward, T. L.: The shallow oxygen maximum layer and primary production, Deep Sea Res. Part Oceanogr. Res. Pap., 41, 559–574, https://doi.org/10.1016/0967-0637(94)90095-7, 1994.

Hersbach, H., Bell, B., Berrisford, P., Hirahara, S., Horányi, A., Muñoz-Sabater, J., Nicolas, J., Peubey, C., Radu, R., Schepers, D., Simmons, A., Soci, C., Abdalla, S., Abellan, X., Balsamo, G., Bechtold, P., Biavati, G., Bidlot, J., Bonavita, M., De Chiara, G., Dahlgren, P., Dee, D., Diamantakis, M., Dragani, R., Flemming, J., Forbes, R., Fuentes, M., Geer, A., Haimberger, L., Healy, S., Hogan, R. J., Hólm, E., Janisková, M., Keeley, S., Laloyaux, P., Lopez, P., Lupu, C., Radnoti, G., de Rosnay, P., Rozum, I., Vamborg, F., Villaume, S., and Thépaut, J.-N.: The ERA5 global reanalysis, Q. J. R. Meteorol. Soc., 146, 1999–2049, https://doi.org/10.1002/qj.3803, 2020.

Hintsa, E. J., Moore, F. L., Hurst, D. F., Dutton, G. S., Hall, B. D., Nance, J. D., Miller, B. R., Montzka, S. A., Wolton, L. P., McClure-Begley, A., Elkins, J. W., Hall, E. G., Jordan, A. F., Rollins, A. W., Thornberry, T. D., Watts, L. A., Thompson, C. R., Peischl, J., Bourgeois, I., Ryerson, T. B., Daube, B. C., Gonzalez Ramos, Y., Commane, R., Santoni, G. W., Pittman, J. V., Wofsy, S. C., Kort, E., Diskin, G. S., and Bui, T. P.: UAS Chromatograph for Atmospheric Trace Species (UCATS) – a versatile instrument for trace gas measurements on airborne platforms, Atmospheric Meas. Tech., 14, 6795–6819, https://doi.org/10.5194/amt-14-6795-2021, 2021.

Huang, S., Shao, J., Chen, Y., Qi, J., Wu, S., Zhang, F., He, X., and Du, Z.: Reconstruction of dissolved oxygen in the Indian Ocean from 1980 to 2019 based on machine learning techniques, Front. Mar. Sci., 10, https://doi.org/10.3389/fmars.2023.1291232, 2023.

Ishidoya, S., Uchida, H., Sasano, D., Kosugi, N., Taguchi, S., Ishii, M., Morimoto, S., Tohjima, Y., Nishino, S., Murayama, S., Aoki, S., Ishijima, K., Fujita, R., Goto, D., and Nakazawa, T.: Ship-based observations of atmospheric potential oxygen and regional air–sea O_2 flux in the northern North Pacific and the Arctic Ocean, Tellus B Chem. Phys. Meteorol., 68, 29972, https://doi.org/10.3402/tellusb.v68.29972, 2016.

Ito, T., Cervania, A., Cross, K., Ainchwar, S., and Delawalla, S.: Mapping Dissolved Oxygen Concentrations by Combining Shipboard and Argo Observations Using Machine Learning Algorithms, J. Geophys. Res. Mach. Learn. Comput., 1, e2024JH000272, https://doi.org/10.1029/2024JH000272, 2024.

Jersild, A., Landschützer, P., Gruber, N., and Bakker, D. C. E.: An observation-based global monthly gridded sea surface pCO_2 and air-sea CO_2 flux product from 1982 onward and its monthly climatology (NCEI Accession 0160558), 2017.

https://doi.org/10.5194/essd-2025-738
Preprint. Discussion started: 23 December 2025

Jin, X., Najjar, R. G., Louanchi, F., and Doney, S. C.: A modeling study of the seasonal oxygen budget of the global ocean, J. Geophys. Res. Oceans, 112, C05017, https://doi.org/10.1029/2006JC003731, 2007.

Jin, Y.: GOBAI-O_2-Flux v1.0: Global Gridded Air-sea Oxygen Flux Inferred from a Machine Learning-based Dissolved Oxygen Product, https://doi.org/10.5281/zenodo.17765275, 2025.

Jin, Y., Keeling, R. F., Morgan, E. J., Ray, E., Parazoo, N. C., and Stephens, B. B.: A mass-weighted isentropic coordinate for mapping chemical tracers and computing atmospheric inventories, Atmospheric Chem. Phys., 21, 217–238, https://doi.org/10.5194/acp-21-217-2021, 2021.

Jin, Y., Stephens, B. B., Keeling, R. F., Morgan, E. J., Rödenbeck, C., Patra, P. K., and Long, M. C.: Seasonal Tropospheric Distribution and Air-Sea Fluxes of Atmospheric Potential Oxygen From Global Airborne Observations, Glob. Biogeochem. Cycles, 37, e2023GB007827, https://doi.org/10.1029/2023GB007827, 2023.

Jin, Y., Stephens, B. B., Long, M. C., Chandra, N., Chevallier, F., Hooghiem, J. J. D., Luijkx, I. T., Maksyutov, S., Morgan, E. J., Niwa, Y., Patra, P. K., Rödenbeck, C., and Vance, J.: The Atmospheric Potential Oxygen forward Model Intercomparison Project (APO-MIP1): evaluating simulated atmospheric transport of air-sea gas exchange tracers and APO flux products, Geosci. Model Dev., 18, 5937–5969, https://doi.org/10.5194/gmd-18-5937-2025, 2025.

Jones, M. W., Andrew, R. M., Peters, G. P., Janssens-Maenhout, G., De-Gol, A. J., Ciais, P., Patra, P. K., Chevallier, F., and Le Quéré, C.: Gridded fossil CO_2 emissions and related O_2 combustion consistent with national inventories 1959–2018, Sci. Data, 8, https://doi.org/10.1038/s41597-020-00779-6, 2021.

Kalnay, E., Kanamitsu, M., Kistler, R., Collins, W., Deaven, D., Gandin, L., Iredell, M., Saha, S., White, G., Woollen, J., Zhu, Y., Chelliah, M., Ebisuzaki, W., Higgins, W., Janowiak, J., Mo, K. C., Ropelewski, C., Wang, J., Leetmaa, A., Reynolds, R., Jenne, R., and Joseph, D.: The NCEP/NCAR 40-Year Reanalysis Project, Bull. Am. Meteorol. Soc., 77, 437–472, https://doi.org/10.1175/1520-0477(1996)077%3C0437:TNYRP%3E2.0.CO;2, 1996.

Keeling, R.: Development of an Interferometric Oxygen Analyzer for Precise Measurement of the Atmospheric O_2 Mole Fraction, Harvard University, 1988.

Keeling, R. F.: Scripps O_2 Program Data. UC San Diego Library Digital Collections, https://doi.org/10.6075/J0WS8RJRs, 2019.

Keeling, R. F. and Garcia, H. E.: The change in oceanic O_2 inventory associated with recent global warming, Proc. Natl. Acad. Sci., 99, 7848–7853, https://doi.org/10.1073/pnas.122154899, 2002.

Keeling, R. F. and Manning, A. C.: Studies of Recent Changes in Atmospheric O_2, in: Treatise on Geochemistry, Elsevier, 385–404, https://doi.org/10.1016/B978-0-08-095975-7.00420-4, 2014.

Keeling, R. F. and Shertz, S. R.: Seasonal and interannual variations in atmospheric oxygen and

https://doi.org/10.5194/essd-2025-738
Preprint. Discussion started: 23 December 2025

implications for the global carbon cycle, Nature, 358, 723–727, https://doi.org/10.1038/358723a0, 1992.

Keeling, R. F., Najjar, R. P., Bender, M. L., and Tans, P. P.: What atmospheric oxygen measurements can tell us about the global carbon cycle, Glob. Biogeochem. Cycles, 7, 37–67, https://doi.org/10.1029/92GB02733, 1993.

Keeling, R. F., Manning, A. C., McEvoy, E. M., and Shertz, S. R.: Methods for measuring changes in atmospheric O_2 concentration and their application in southern hemisphere air, J. Geophys. Res. Atmospheres, 103, 3381–3397, https://doi.org/10.1029/97JD02537, 1998a.

Keeling, R. F., Stephens, B. B., Najjar, R. G., Doney, S. C., Archer, D., and Heimann, M.: Seasonal variations in the atmospheric O_2/N_2 ratio in relation to the kinetics of air-sea gas exchange, Glob. Biogeochem. Cycles, 12, 141–163, https://doi.org/10.1029/97GB02339, 1998b.

Keeling, R. F., Blaine, T., Paplawsky, B., Katz, L., Atwood, C., and Brockwell, T.: Measurement of changes in atmospheric Ar/N_2 ratio using a rapid-switching, single-capillary mass spectrometer system, Tellus B, 56, 322–338, https://doi.org/10.1111/j.1600-0889.2004.00117.x, 2004.

Keeling, R. F., Manning, A. C., Paplawsky, W. J., and Cox, A. C.: On the long-term stability of reference gases for atmospheric O2/N2 and CO2 measurements, Tellus B Chem. Phys. Meteorol., 59, 3–14, https://doi.org/10.1111/j.1600-0889.2006.00196.x, 2007.

Keeling, R. F., Körtzinger, A., and Gruber, N.: Ocean Deoxygenation in a Warming World, Annu. Rev. Mar. Sci., 2, 199–229, https://doi.org/10.1146/annurev.marine.010908.163855, 2010.

Keeling, R. F., Walker, S. J., and Paplawsky, W.: Span Sensitivity of the Scripps Interferometric Oxygen Analyzer, 2020.

Koelling, J., Atamanchuk, D., Karstensen, J., Handmann, P., and Wallace, D. W. R.: Oxygen export to the deep ocean following Labrador Sea Water formation, Biogeosciences, 19, 437–454, https://doi.org/10.5194/bg-19-437-2022, 2022.

Kosaka, Y., Kobayashi, S., Harada, Y., Kobayashi, C., Naoe, H., Yoshimoto, K., Harada, M., Goto, N., Chiba, J., Miyaoka, K., Sekiguchi, R., Deushi, M., Kamahori, H., Nakaegawa, T., Tanaka, T. Y., Tokuhiro, T., Sato, Y., Matsushita, Y., and Onogi, K.: The JRA-3Q Reanalysis, J. Meteorol. Soc. Jpn. Ser II, 102, 49–109, https://doi.org/10.2151/jmsj.2024-004, 2024.

Landschützer, P., Gruber, N., and Bakker, D. C. E.: Decadal variations and trends of the global ocean carbon sink, Glob. Biogeochem. Cycles, 30, 1396–1417, https://doi.org/10.1002/2015GB005359, 2016.

Levitus, S., Antonov, J. I., Boyer, T. P., Baranova, O. K., Garcia, H. E., Locarnini, R. A., Mishonov, A. V., Reagan, J. R., Seidov, D., Yarosh, E. S., and Zweng, M. M.: World ocean heat content and thermosteric sea level change (0–2000 m), 1955–2010, Geophys. Res. Lett., 39, 2012GL051106, https://doi.org/10.1029/2012GL051106, 2012.

https://doi.org/10.5194/essd-2025-738
Preprint. Discussion started: 23 December 2025

Levitus, S., Antonov, J., Boyer, T. P., Baranova, O. K., Garcia, H. E., Locarnini, R. A., Alexey, V., Reagan, J. R., Seidov, D., Yarosh, Evgeney, and Zweng, M. M.: NCEI ocean heat content, temperature anomalies, salinity anomalies, thermosteric sea level anomalies, halosteric sea level anomalies, and total steric sea level anomalies from 1955 to present calculated from in situ oceanographic subsurface profile data (NCEI Accession 0164586). Accessed 2025-11-14, https://doi.org/10.7289/v53f4mvp., 2017.

Li, C., Huang, J., Liu, X., Ding, L., He, Y., and Xie, Y.: The ocean losing its breath under the heatwaves, Nat. Commun., 15, 6840, https://doi.org/10.1038/s41467-024-51323-8, 2024.

Liang, J., Deutsch, C., McWilliams, J. C., Baschek, B., Sullivan, P. P., and Chiba, D.: Parameterizing bubble-mediated air-sea gas exchange and its effect on ocean ventilation, Glob. Biogeochem. Cycles, 27, 894–905, https://doi.org/10.1002/gbc.20080, 2013.

Manizza, M., Keeling, R. F., and Nevison, C. D.: On the processes controlling the seasonal cycles of the air–sea fluxes of O_2 and N_2O: A modelling study, Tellus B Chem. Phys. Meteorol., 64, 18429, https://doi.org/10.3402/tellusb.v64i0.18429, 2012.

Mears, C., Lee, T., Ricciardulli, L., Wang, X., and Wentz, F.: Improving the Accuracy of the Cross-Calibrated Multi-Platform (CCMP) Ocean Vector Winds, Remote Sens., 14, 4230, https://doi.org/10.3390/rs14174230, 2022.

Najjar, R. G. and Keeling, R. F.: Analysis of the mean annual cycle of the dissolved oxygen anomaly in the World Ocean, J. Mar. Res., 55, 117–151, https://doi.org/10.1357/0022240973224481, 1997.

Najjar, R. G. and Keeling, R. F.: Mean annual cycle of the air-sea oxygen flux: A global view, Glob. Biogeochem. Cycles, 14, 573–584, https://doi.org/10.1029/1999GB900086, 2000.

Niwa, Y., Tomita, H., Satoh, M., and Imasu, R.: A Three-Dimensional Icosahedral Grid Advection Scheme Preserving Monotonicity and Consistency with Continuity for Atmospheric Tracer Transport, J. Meteorol. Soc. Jpn. Ser II, 89, 255–268, https://doi.org/10.2151/jmsj.2011-306, 2011.

Olsen, A., Key, R. M., van Heuven, S., Lauvset, S. K., Velo, A., Lin, X., Schirnick, C., Kozyr, A., Tanhua, T., Hoppema, M., Jutterström, S., Steinfeldt, R., Jeansson, E., Ishii, M., Pérez, F. F., and Suzuki, T.: The Global Ocean Data Analysis Project version 2 (GLODAPv2) – an internally consistent data product for the world ocean, Earth Syst. Sci. Data, 8, 297–323, https://doi.org/10.5194/essd-8-297-2016, 2016.

Patra, P. K., Takigawa, M., Watanabe, S., Chandra, N., Ishijima, K., and Yamashita, Y.: Improved Chemical Tracer Simulation by MIROC4.0-based Atmospheric Chemistry-Transport Model (MIROC4-ACTM), SOLA, 14, 91–96, https://doi.org/10.2151/sola.2018-016, 2018.

Pickers, P. A., Manning, A. C., Sturges, W. T., Le Quéré, C., Mikaloff Fletcher, S. E., Wilson, P. A., and Etchells, A. J.: In situ measurements of atmospheric O_2 and CO_2 reveal an unexpected O_2 signal over the tropical Atlantic Ocean, Glob. Biogeochem. Cycles, 31, 1289–1305, https://doi.org/10.1002/2017GB005631, 2017.

https://doi.org/10.5194/essd-2025-738
Preprint. Discussion started: 23 December 2025

Rayner, N. A., Parker, D. E., Horton, E. B., Folland, C. K., Alexander, L. V., Rowell, D. P., Kent, E. C., and Kaplan, A.: Global analyses of sea surface temperature, sea ice, and night marine air temperature since the late nineteenth century, J. Geophys. Res. Atmospheres, 108, 2002JD002670, https://doi.org/10.1029/2002JD002670, 2003.

Redfield, A. C.: The Exchange Of Oxygen Across The sea Surface, J. Mar. Res., 7, 347–361, 1948.

Resplandy, L., Keeling, R. F., Stephens, B. B., Bent, J. D., Jacobson, A., Rödenbeck, C., and Khatiwala, S.: Constraints on oceanic meridional heat transport from combined measurements of oxygen and carbon, Clim. Dyn., 47, 3335–3357, https://doi.org/10.1007/s00382-016-3029-3, 2016.

Resplandy, L., Keeling, R. F., Eddebbar, Y., Brooks, M., Wang, R., Bopp, L., Long, M. C., Dunne, J. P., Koeve, W., and Oschlies, A.: Quantification of ocean heat uptake from changes in atmospheric O_2 and CO_2 composition, Sci. Rep., 9, 20244, https://doi.org/10.1038/s41598-019-56490-z, 2019.

Roach, C. J. and Bindoff, N. L.: Developing a New Oxygen Atlas of the World's Oceans Using Data Interpolating Variational Analysis, J. Atmospheric Ocean. Technol., 40, 1475–1491, https://doi.org/10.1175/JTECH-D-23-0007.1, 2023.

Rödenbeck, C., Quéré, C. L., Heimann, M., and Keeling, R. F.: Interannual variability in oceanic biogeochemical processes inferred by inversion of atmospheric O_2/N_2 and CO_2 data, Tellus B Chem. Phys. Meteorol., 60, 685–705, https://doi.org/10.1111/j.1600-0889.2008.00375.x, 2008.

Roemmich, D. and Gilson, J.: The 2004–2008 mean and annual cycle of temperature, salinity, and steric height in the global ocean from the Argo Program, Prog. Oceanogr., 82, 81–100, https://doi.org/10.1016/j.pocean.2009.03.004, 2009.

Santoni, G. W., Daube, B. C., Kort, E. A., Jiménez, R., Park, S., Pittman, J. V., Gottlieb, E., Xiang, B., Zahniser, M. S., Nelson, D. D., McManus, J. B., Peischl, J., Ryerson, T. B., Holloway, J. S., Andrews, A. E., Sweeney, C., Hall, B., Hintsa, E. J., Moore, F. L., Elkins, J. W., Hurst, D. F., Stephens, B. B., Bent, J., and Wofsy, S. C.: Evaluation of the airborne quantum cascade laser spectrometer (QCLS) measurements of the carbon and greenhouse gas suite – CO_2, CH_4, N_2O, and CO – during the CalNex and HIPPO campaigns, Atmospheric Meas. Tech., 7, 1509–1526, https://doi.org/10.5194/amt-7-1509-2014, 2014.

Satoh, M., Tomita, H., Yashiro, H., Miura, H., Kodama, C., Seiki, T., Noda, A. T., Yamada, Y., Goto, D., Sawada, M., Miyoshi, T., Niwa, Y., Hara, M., Ohno, T., Iga, S., Arakawa, T., Inoue, T., and Kubokawa, H.: The Non-hydrostatic Icosahedral Atmospheric Model: description and development, Prog. Earth Planet. Sci., 1, 18, https://doi.org/10.1186/s40645-014-0018-1, 2014.

Schmidtko, S., Stramma, L., and Visbeck, M.: Decline in global oceanic oxygen content during the past five decades, Nature, 542, 335–339, https://doi.org/10.1038/nature21399, 2017.

Schott, F. A. and McCreary, J. P.: The monsoon circulation of the Indian Ocean, Prog. Oceanogr., 51, 1–123, https://doi.org/10.1016/S0079-6611(01)00083-0, 2001.

https://doi.org/10.5194/essd-2025-738
Preprint. Discussion started: 23 December 2025

Schuldt, K. N., Mund, J., Luijkx, I. T., Aalto, T., Abshire, J. B., Aikin, K., Andrews, A., Aoki, S., Apadula, F., Baier, B., Bakwin, P., Bartyzel, J., Bentz, G., Bergamaschi, P., Beyersdorf, A., Biermann, T., Biraud, S. C., Boenisch, H., Bowling, D., Brailsford, G., Chen, G., Chen, H., Chmura, L., Clark, S., Climadat, S., Colomb, A., Commane, R., Conil, S., Cox, A., Cristofanelli, P., Cuevas, E., Curcoll, R., Daube, B., Davis, K., De Mazière, M., De Wekker, S., Della Coletta, J., Delmotte, M., DiGangi, J. P., Dlugokencky, E., Elkins, J. W., Emmenegger, L., Fang, S., Fischer, M. L., Forster, G., Frumau, A., Galkowski, M., Gatti, L. V., Gehrlein, T., Gerbig, C., Gheusi, F., Gloor, E., Gomez-Trueba, V., Goto, D., Griffis, T., Hammer, S., Hanson, C., Haszpra, L., Hatakka, J., Heimann, M., Heliasz, M., Hensen, A., Hermanssen, O., Hintsa, E., Holst, J., Ivakhov, V., Jaffe, D., Joubert, W., Karion, A., Kawa, S. R., Kazan, V., Keeling, R., Keronen, P., Kolari, P., Kominkova, K., Kort, E., Kozlova, E., Krummel, P., Kubistin, D., Labuschagne, C., Lam, D. H., Langenfelds, R., Laurent, O., Laurila, T., Lauvaux, T., Lavric, J., Law, B., Lee, O. S., Lee, J., Lehner, I., Leppert, R., Leuenberger, M., Levin, I., Levula, J., Lin, J., Lindauer, M., Loh, Z., Lopez, M., Machida, T., et al.: Multi-laboratory compilation of atmospheric carbon dioxide data for the period 1957-2020; obspack_co2_1_GLOBALVIEWplus_v7.0_2021-08-18, , https://doi.org/10.25925/20210801, 2021.

Severinghaus, J.: Studies of the terrestrial O_2 and carbon cycles in sand dune gases and in Biosphere 2, Columbia University, 1995.

Sharp, data, Fassbender, A. J., Carter, B. R., Johnson, G. C., Schultz, C., and Dunne, J. P.: GOBAI-O_2 : temporally and spatially resolved fields of ocean interior dissolved oxygen over nearly 2 decades, Earth Syst. Sci. Data, 15, 4481–4518, https://doi.org/10.5194/essd-15-4481-2023, 2023.

Sharp, J. D., Fassbender, A. J., Carter, B. R., Johnson, G. C., Schultz, C., and Dunne, J. P.: GOBAI-O₂: A Global Gridded Monthly Dataset of Ocean Interior Dissolved Oxygen Concentrations Based on Shipboard and Autonomous Observations (NCEI Accession 0259304). NOAA National Centers for Environmental Information. Accessed 2024-11-12, https://doi.org/10.25921/z72m-yz67, 2022.

Sharp, J. D., Fassbender, A. J., Carter, B. R., Johnson, G. C., Dunne, J. P., and Schultz, C.: GOBAI-O_2: A Global Gridded Monthly Dataset of Ocean Interior Dissolved Oxygen Concentrations Based on Shipboard and Autonomous Observations (NCEI Accession 0259304). NOAA National Centers for Environmental Information. [Last Access: 2025-10-28], https://doi.org/10.25921/z72m-yz67, 2025.

Silva, A. N., Purdie, D. A., Bates, N. R., and Tyrrell, T.: Investigating Labrador Sea's persistent surface O2 anomaly using observations and biogeochemical model results, J. Mar. Syst., 245, 103996, https://doi.org/10.1016/j.jmarsys.2024.103996, 2024.

Stanley, R. H. R., Jenkins, W. J., Lott III, D. E., and Doney, S. C.: Noble gas constraints on air-sea gas exchange and bubble fluxes, J. Geophys. Res. Oceans, 114, https://doi.org/10.1029/2009JC005396, 2009.

Steinbach, J., Gerbig, C., Rödenbeck, C., Karstens, U., Minejima, C., and Mukai, H.: The CO_2 release and Oxygen uptake from Fossil Fuel Emission Estimate (COFFEE) dataset: effects from

https://doi.org/10.5194/essd-2025-738
Preprint. Discussion started: 23 December 2025

varying oxidative ratios, Atmospheric Chem. Phys., 11, 6855–6870, https://doi.org/10.5194/acp-11-6855-2011, 2011.

Stephens, B.: ORCAS Merge Products. Version 1.0. UCAR/NCAR - Earth Observing Laboratory, https://doi.org/10.5065/D6SB445X., 2017.

Stephens, B., Keeling, R., Bent, J., Watt, A., Shertz, S., and Paplawsky, W.: HIPPO-1 airborne oxygen instrument. Version 2.0. UCAR/NCAR—Earth Observing Laboratory., https://doi.org/10.5065/D6J38QVV, 2021a.

Stephens, B., Keeling, R., Bent, J., Watt, A., Shertz, S., and Paplawsky, W.: HIPPO-2 airborne oxygen instrument. Version 2.0. UCAR/NCAR—Earth Observing Laboratory., https://doi.org/10.5065/D65Q4TF0, 2021b.

Stephens, B., Keeling, R., Bent, J., Watt, A., Shertz, S., and Paplawsky, W.: HIPPO-3 airborne oxygen instrument. Version 2.0. UCAR/NCAR—Earth Observing Laboratory., https://doi.org/10.5065/D67H1GXJ, 2021c.

Stephens, B., Keeling, R., Bent, J., Watt, A., Shertz, S., and Paplawsky, W.: HIPPO-4 airborne oxygen instrument. Version 2.0. UCAR/NCAR—Earth Observing Laboratory., https://doi.org/10.5065/D679431D, 2021d.

Stephens, B., Keeling, R., Bent, J., Watt, A., Shertz, S., and Paplawsky, W.: HIPPO-5 airborne oxygen instrument. Version 2.0. UCAR/NCAR—Earth Observing Laboratory., https://doi.org/10.5065/D6WW7G0D, 2021e.

Stephens, B., Keeling, R., Bent, J., Watt, A., Shertz, S., and Paplawsky, W.: ORCAS Airborne Oxygen Instrument. Version 2.0. UCAR/NCAR - Earth Observing Laboratory., https://doi.org/10.5065/D6N29VC6, 2021f.

Stephens, B., Long, M., Jin, Y., Chandra, N., Chevallier, F., Hooghiem, J., Luijkx, I., Maksyutov, S., Morgan, E., Niwa, Y., Patra, P., Rodenbeck, C., and Vance, J.: Atmospheric Potential Oxygen forward Model Intercomparison Project (APO-MIP), https://doi.org/10.5065/F3PW-A676, 2025.

Stephens, B. B.: ARSV Laurence M. Gould Atmospheric O_2 and CO_2 Measurements. Version 1.0. UCAR/NCAR - Earth Observing Laboratory, https://doi.org/10.26023/FDDD-PC3X-4M0X, 2025.

Stephens, B. B., Keeling, R. F., Heimann, M., Six, K. D., Murnane, R., and Caldeira, K.: Testing global ocean carbon cycle models using measurements of atmospheric O_2 and CO_2 concentration, Glob. Biogeochem. Cycles, 12, 213–230, https://doi.org/10.1029/97GB03500, 1998.

Stephens, B. B., Long, M. C., Keeling, R. F., Kort, E. A., Sweeney, C., Apel, E. C., Atlas, E. L., Beaton, S., Bent, J. D., Blake, N. J., Bresch, J. F., Casey, J., Daube, B. C., Diao, M., Diaz, E., Dierssen, H., Donets, V., Gao, B.-C., Gierach, M., Green, R., Haag, J., Hayman, M., Hills, A. J., Hoecker-Martínez, M. S., Honomichl, S. B., Hornbrook, R. S., Jensen, J. B., Li, R.-R., McCubbin, I., McKain, K., Morgan, E. J., Nolte, S., Powers, J. G., Rainwater, B., Randolph, K.,

https://doi.org/10.5194/essd-2025-738
Preprint. Discussion started: 23 December 2025

Reeves, M., Schauffler, S. M., Smith, K., Smith, M., Stith, J., Stossmeister, G., Toohey, D. W., and Watt, A. S.: The O_2/N_2 Ratio and CO_2 Airborne Southern Ocean Study, Bull. Am. Meteorol. Soc., 99, 381–402, https://doi.org/10.1175/BAMS-D-16-0206.1, 2018.

Stephens, B. B., Morgan, E. J., Bent, J. D., Keeling, R. F., Watt, A. S., Shertz, S. R., and Daube, B. C.: Airborne measurements of oxygen concentration from the surface to the lower stratosphere and pole to pole, Atmospheric Meas. Tech., 14, 2543–2574, https://doi.org/10.5194/amt-14-2543-2021, 2021g.

Thompson, C., Wofsy, S. C., Prather, M. J., Newman, P. A., Hanisco, T. F., Ryerson, T. B., Fahey, D. W., Apel, E. C., Brock, C. A., Brune, W. H., Froyd, K., Katich, J. M., Nicely, J. M., Peischl, J., Ray, E., Veres, P. R., Wang, S., Allen, H. M., Asher, E., Bian, H., Blake, D., Bourgeois, I., Budney, J., Bui, T. P., Butler, A., Campuzano-Jost, P., Chang, C., Chin, M., Commane, R., Correa, G., Crounse, J. D., Daube, B., Dibb, J. E., DiGangi, J. P., Diskin, G. S., Dollner, M., Elkins, J. W., Fiore, A. M., Flynn, C. M., Guo, H., Hall, S. R., Hannun, R. A., Hills, A., Hintsa, E. J., Hodzic, A., Hornbrook, R. S., Huey, L. G., Jimenez, J. L., Keeling, R. F., Kim, M. J., Kupc, A., Lacey, F., Lait, L. R., Lamarque, J.-F., Liu, J., McKain, K., Meinardi, S., Miller, D. O., Montzka, S. A., Moore, F. L., Morgan, E. J., Murphy, D. M., Murray, L. T., Nault, B. A., Neuman, J. A., Nguyen, L., Gonzalez, Y., Rollins, A., Rosenlof, K., Sargent, M., Schill, G., Schwarz, J. P., Clair, J. M. St., Steenrod, S. D., Stephens, B. B., Strahan, S. E., Strode, S. A., Sweeney, C., Thames, A. B., Ullmann, K., Wagner, N., Weber, R., Weinzierl, B., Wennberg, P. O., Williamson, C. J., Wolfe, G. M., and Zeng, L.: The NASA Atmospheric Tomography (ATom) Mission: Imaging the Chemistry of the Global Atmosphere, Bull. Am. Meteorol. Soc., 103, E761–E790, https://doi.org/10.1175/BAMS-D-20-0315.1, 2022.

Tohjima, Y., Minejima, C., Mukai, H., Machida, T., Yamagishi, H., and Nojiri, Y.: Analysis of seasonality and annual mean distribution of atmospheric potential oxygen (APO) in the Pacific region, Glob. Biogeochem. Cycles, 26, 2011GB004110, https://doi.org/10.1029/2011GB004110, 2012.

Walker, N. D., Leben, R. R., and Balasubramanian, S.: Hurricane-forced upwelling and chlorophyll a enhancement within cold-core cyclones in the Gulf of Mexico, Geophys. Res. Lett., 32, L18610, https://doi.org/10.1029/2005GL023716, 2005.

Wanninkhof, R.: Relationship between wind speed and gas exchange over the ocean revisited, Limnol. Oceanogr. Methods, 12, 351–362, https://doi.org/10.4319/lom.2014.12.351, 2014.

Watanabe, S., Miura, H., Sekiguchi, M., Nagashima, T., Sudo, K., Emori, S., and Kawamiya, M.: Development of an Atmospheric General Circulation Model for Integrated Earth System Modeling on the Earth Simulator, J. Earth Simulator, 9, 27–35, https://doi.org/10.32131/jes.9.27, 2008.

Weiss, R. F.: The solubility of nitrogen, oxygen and argon in water and seawater, Deep Sea Res. Oceanogr., 17, 721–735, https://doi.org/10.1016/0011-7471(70)90037-9, 1970.

Wofsy, S.: ATom: Merged atmospheric chemistry, trace gases, and aerosols, version 2 (version 2.0). ORNL Distributed Active Archive Center., https://doi.org/10.3334/ORNLDAAC/1925, 2021.

https://doi.org/10.5194/essd-2025-738
Preprint. Discussion started: 23 December 2025

1602 Wofsy, S. C.: HIAPER Pole-to-Pole Observations (HIPPO): fine-grained, global-scale
1603 measurements of climatically important atmospheric gases and aerosols, Philos. Trans. R. Soc.
1604 A, 369, 2073–2086, https://doi.org/10.1098/rsta.2010.0313, 2011.

1605 Wofsy, S. C.: HIPPO merged 10-second meteorology, atmospheric chemistry, and aerosol data.
1606 Version 1.0. UCAR/NCAR - Earth Observing Laboratory.,
1607 https://doi.org/10.3334/CDIAC/HIPPO_010, 2017.

1608 Woolf, D. K.: Bubbles and their role in gas exchange, in: The Sea Surface and Global Change,
1609 edited by: Liss, P. S. and Duce, R. A., Cambridge University Press, 173–206,
1610 https://doi.org/10.1017/CBO9780511525025.007, 1997.

1611 Woolf, D. K. and Thorpe, S. A.: Bubbles and the air-sea exchange of gases in near-saturation
1612 conditions, J. Mar. Res., 49, 435–466, https://doi.org/10.1357/002224091784995765, 1991.

1613 Yeager, S. G., Rosenbloom, N., Glanville, A. A., Wu, X., Simpson, I., Li, H., Molina, M. J.,
1614 Krumhardt, K., Mogen, S., Lindsay, K., Lombardozzi, D., Wieder, W., Kim, W. M., Richter, J.
1615 H., Long, M., Danabasoglu, G., Bailey, D., Holland, M., Lovenduski, N., Strand, W. G., and
1616 King, T.: The Seasonal-to-Multiyear Large Ensemble (SMYLE) prediction system using the
1617 Community Earth System Model version 2, Geosci. Model Dev., 15, 6451–6493,
1618 https://doi.org/10.5194/gmd-15-6451-2022, 2022.

1619 Zhou, Y., Gong, H., and Zhou, F.: Responses of Horizontally Expanding Oceanic Oxygen
1620 Minimum Zones to Climate Change Based on Observations, Geophys. Res. Lett., 49,
1621 e2022GL097724, https://doi.org/10.1029/2022GL097724, 2022.